SLAC-PUB-2648 (Rev.)
November 1980
April 1981 (Rev.)
(M)

APPLICATION OF THE METHOD OF MONTE CARLO TO COMPTON SCATTERING RADIOGRAPHY IN HOMOGENEOUS MEDIA *

A. Del Guerra, R. Bellazzini, G. Tonelli and R. Venturi
Istituto di Fisica dell Universita', Piazza Torricelli, 2
I-56100 Pisa, Italy

and

Istituto Nazionale di Fisica Nucleare, Sezione di Pisa,
S. Piero a Grado, I-56010 Pisa, Italy

and

W. R. Nelson†
Stanford Linear Accelerator Center
P. O. Box 4349
Stanford, California 94305, U.S.A.

Submitted to Physics in Medicine and Biology

---

* Work supported in part by the Department of Energy under contract number DE-AC03-76SF00515, and in part by the Health and Safety Division at CERN.

† Partially supported by the Health and Safety Division at CERN during leave of absence from SLAC, 1978-1979.

ABSTRACT

It has recently been proposed that 90^{o} Compton scattering from a planar monoenergetic gamma source can be used as a diagnostic tool for tomographic studies of the lung. In this paper we present a detailed Monte Carlo study of the performance that can be obtained with this technique for homogeneous media, as a function of both the incident photon energy and the source-detector geometry. A 20 x 20 x 20 cm^3 water phantom was simulated as a target and a conventional gamma camera equipped with imaging collimator as a detector. The multiple to single scatter ratio was found to have an approximate 1/E dependence with the energy of the incident photon; its magnitude (as high as 70% for a 279 keV gamma source) is mostly determined by the finite energy resolution of the detector. The multiple scattering contamination as a function of the depth into the phantom was also studied in order to derive algorithms that can be applied to clinical data. The Monte Carlo calculations agree to a few percent with experimental data.

1. Introduction

The purpose of this study is to simulate, by Monte Carlo methods, Compton scattering radiography in an experimental configuration never before simulated; namely, for a gamma camera and imaging collimator detecting 90° scattered photons from a line source incident on a phantom. In particular, we have studied the multiple scattering contamination of the single scattering signal in such a way as to provide information that 1) can be used to correct actual clinical data, and 2) establishes the limits of Compton radiography in terms of the detector used. In addition, the computer programs that we have developed are significantly faster and provide much more information about intrinsic details occurring in the radiation transport than codes previously used by others. The latter is particularly important for future studies involving complex three dimensional heterogeneous phantoms, where simple analytic calculations will not suffice.

The use of Compton scattered radiation to produce an image of a selected volume of human tissue for diagnostic purposes was originally proposed by Lale (1959) and Clarke (1965). The principle of this technique is to irradiate a biological target with a narrow monenergetic X- or gamma-ray beam and to detect the fluence of scattered photons into a well defined solid angle in order to obtain information on the mass density of the target. The fluence of scattered photons, in fact, depends linearly upon the electron density of the target; the latter is related to the mass density provided that the value of Z/A (weighted average) is known. Using two body kinematics, one can determine the scattered photon energy, E', for the Compton process from

$$E' = E/[1 + (1-\cos\theta)E/m_oc^2], \qquad (1)$$

where E is the incident photon energy, m_oc^2 is the rest mass energy of the electron, and θ is the angle of the scattered photon in the laboratory. This expression may be used as a constraint in order to isolate the signal (i.e., single Compton scatter) from the background and, therefore, assists in the reconstruction of the mass density of the irradiated volume.

The first prototypes of Compton scanners built for medical application made use of an external MV X-ray source (Lale 1968), or a ^{60}Co source (Clarke and Van Dyk 1969) collimated to a narrow beam into the target. A collimator in front of the crystal detector subtended a definite solid angle at the target, centered at a scattering angle ranging from 30 to 120°. A scanning of the beam through the target thus allowed the reconstruction of the whole three dimensional picture of the irradiated volume. A long scanning time was necessary to produce a complete image of a section of the human body, and a high dose (approximately 0.1 Gy) was required in order to achieve a still rather poor electron density resolution (less than 10%). It has been understood from the beginning that the main limitations to the density resolution derive from the attenuation of the incident beam and from the contamination introduced by multiple scattering by the photons in the target. The latter produces a "fake" signal in the detector, one that arises from a volume in the target other than the irradiated one. Thus, the information on the mass density of the selected volume is altered by the material around it.

In order to improve the signal to noise ratio caused by multiple scattering, Farmer and Collins (1971, 1974) used a ^{137}Cs narrow beam source and two Ge(Li) detectors centered at 90° to the incident beam. Even though the Ge(Li) detectors provided an improvement of the energy resolution, the size of the detectors that were available limited the sensitivity and, therefore, again affected the signal to noise ratio.

The recent popularity of Transmission CT-scanners (TCT) during the last decade has overshadowed this technique as a means of performing whole body tomography. Still, several attempts have been made to exploit Compton scanners, although most have been densitometry studies. Original work in this field has been done by Zelefsky and Schulz (1968) for ventilation studies of the lung, by Reiss et al (1972), Dohring et al (1974), and Kaufman et al (1976) for in vivo measurements of lung density inhomogeneity, and by Garret et al (1973), Clarke and Van Dyk (1973), Webber and Kennett (1976), Kennett and Webber (1976), and Hazan et al (1977) for bone densitometry. Experiments have been performed in order to measure the electron density of a small volume (few cm^3) by using a narrow beam geometry and a small solid angle detector. An accuracy of a few percent in the determination of the electron density has been achieved for a dose less than 0.01 Gy.

The reason for such an interest is mainly due to the fact that the information on electron density obtainable with conventional TCT scanners will reflect the photoelectric contribution to the absorption coefficient. Although dual-energy TCT scanners have been used to unfold the photoelectric effect contribution (Rutherford et al 1976a,b, Kelcz 1979, Talbert et al 1980), the reproducibility of present dual-energy TCT scanners is not adequate enough for long term repeated studies (e.g., early detection of osteoporosis). On the other hand, the image produced by means of a Compton scanner reflects only the Compton contribution and, therefore, is directly related to the electron density, even if additional artifacts are introduced by attenuation and by multiple scattering. Hence, Compton scanners seem to provide a powerful instrument for densitometry studies, once those artifacts are removed or considerably reduced by means of a better geometry and a more suitable detector.

Compton scanners have also been proposed as a tool to aid in treatment planning. In this case, dose limitations are less critical and Compton scanners may be competitive with TCT scanners. An electron density accuracy of 5% and a spatial resolution of 0.5 cm for tissue inhomogeneities is required for a 3% accuracy in the absorbed dose calculation for treatment planning with MV X-rays (Geise and McCullough 1977, Sontag et al 1977). To achieve the same or better resolution using Compton scanners, one must first account for the two main sources of perturbation: attenuation and multiple scattering.

Battista and Bronskill (1978) first tried to evaluate these two effects both analytically and using Monte Carlo techniques. They considered a narrow beam of photons, having energies between 300 and 2000 keV, incident on either a cylindrical or parallelepiped target. A Clarke-type scanner was taken as the detector. The Monte Carlo program, written in FORTRAN, took as much as 0.125 seconds per photon history on a PDP-11/55 computer. Nonetheless, the results that were obtained agreed rather well with experimental data (Battista et al 1977). They conclude from their experimental results that transverse images with an electron density accuracy of approximately 5% are possible.

A combined version of TCT scanner and Compton scanner has been proposed by Leunbach (1977). This method, referred to as "linear computer-assisted tomography", uses a narrow beam ^{137}Cs source that is rotated together with a detector to measure the transmitted beam. A fixed annular ring detector is used for measuring the scattered radiation. A density resolution of approximately 0.5%, a spatial resolution of better than 4 mm, and a dose of less than 0.03 Gy, for a scanning time for 150 seconds, have been quoted for a tomographic image of a cross section of the human body.

More recently, several applications have been made of the Compton scattering technique, which make use of a large-field gamma camera equipped with an imaging collimator as a detector (Mirell et al 1977, Guzzardi et al 1977, 1978, Pistolesi et al 1977, 1978, Endo et al 1979). All of these applications use gamma cameras, equipped with high resolution imaging collimators to improve background rejection (e.g., see Eqn. (1)), positioned 90° relative to the irradiating source.

The use of a large NaI(Tl) crystal of small thickness (typically 1.25 cm) requires choosing a low energy gamma source in order to obtain a reasonable efficiency with such gamma cameras. In order to overcome the difficulty of a long scanning time, a planar source is chosen (as opposed to a narrow beam), thereby providing uniform irradiation of the whole slice of interest in a single exposure. Several types of source geometries have been tried; for example, a linear ^{203}Hg source, a double linear ^{203}Hg source (Giuntini et al 1979), a rotating "fan" beam of ^{192}Ir photons, and an ^{192}Ir dipole source (Guzzardi 1980) have been used.

Applications developed at the CNR Institute of Clinical Physiology (Guzzardi et al 1977, 1978, Pistolesi et al 1977, 1978, Giuntini et al 1979) for tomographic studies of the lung are of particular interest because of the relatively low doses involved (about 0.5 mGy at the skin for each tomographic study). These techniques are applicable for routine studies, as well as for continuous monitoring of patients who cannot be transported to a conventional TCT scanner (e.g., those with pulmonary edema).

An attempt has recently been made to correct the experimental image for attenuation of the incident beam (Bellazzini et al 1978). However, it became quite apparent that the multiple scattering contribution had to be better understood. Consequently, a comparative study was initiated for various source geometries and incident energies, the results of which are the subject of the current paper. We present the results of a detailed Monte Carlo calculation performed to study single (S) and multiple (M) Compton scattering at 90°, both as a function of the detector resolution (energy and spatial) and the source geometry, at various incident energies (preliminary results have already been reported by Bellazzini et al 1979). The ratio, M/S, as a function of target depth in homogeneous media, is discussed. Finally, a comparison of our Monte Carlo results with expermental data is presented for the case of a sawdust phantom irradiated by a collimated line source of ^{203}Hg.

In a subsequent paper, we will present results on the Compton radiography of inhomogeneous phantoms and the effect of irradiating the phantom laterally off-axis. An estimate of the absorbed dose to the phantom will also be made in that paper.

2. Monte Carlo Technique and Problem Model

2.1 *The EGS Monte Carlo Program: General Description and the EGS User Code Concept*

For the simulation of Compton scattering from a phantom, a general electromagnetic radiation transport code called EGS (Electron-Gamma Shower), written by Ford and Nelson (1978), was used. The EGS code is written in an extended FORTRAN language known as MORTRAN (Cook and Shustek 1975) and is currently being used by several hundred different users to solve a variety of problems in accelerator, high-energy, and medical physics (Nelson and Jenkins 1980). In particular, EGS is capable of treating electrons, positrons, and photons with kinetic energies as high as 3000 GeV and as low as 1 keV (photons) and 1 MeV (electrons and positrons). The transport can take place in any of 100 different elements, or in any mixture or compound of these elements. It is left up to the user to construct his own geometry and to score a particular answer, which has led to a vast assortment of complex simulations of late (Nelson and Jenkins 1980). For the problem at hand, information concerning event by event Compton scattering is required and EGS is well-suited for this task.

The computational portion of the EGS Code System is divided into two parts. First, a preprocessor code (PEGS) uses theoretical (and sometimes empirical) formulas to compute the various physical quantities needed (e.g., cross sections, branching ratios, etc.) and prepares them in a form suitable for fast numerical evaluation. Then the EGS code itself uses this data, along with user supplied data and routines, to perform the actual simulation.

As shown in Fig. 1, the EGS code consists of two "user-callable" subroutines, HATCH and SHOWER, which in turn call the other subroutines in the EGS code --- some of which call two "user-written" subroutines, HOWFAR and AUSGAB. The latter determine the geometry and output (i.e., scoring), respectively. The user communicates with EGS by means of various COMMON variables. To use EGS, the user must write a MAIN program and the subroutines HOWFAR and AUSGAB. Usually, MAIN will perform any initialization needed for HOWFAR and/or AUSGAB, and will set the values of certain EGS COMMON variables which specify such things as names of the media to be used, the desired cutoff energies, and unit of distance (e.g., centimeters, radiation lengths, etc.). MAIN then calls the HATCH subroutine which "hatches" EGS by doing necessary once-only initialization and by reading the material data prepared (earlier) by PEGS for the media requested. With this initialization completed, MAIN then calls SHOWER as many times as desired. Each call to SHOWER results in the generation of one Electron-Gamma Shower history. Thus the user has the freedom to use any source distribution he desires. Figure 1 illustrates the flow of control and data when a user-written program (called a "User Code") interfaces with the EGS code.

2.2 *The Compton Scattering User Code, UCPISA*

As previously stated, the user communicates with the EGS code by means of MAIN and the subroutines HOWFAR (to specify the geometry) and AUSGAB (to score and output results). In addition, the macro-facility of MORTRAN (Cook and Shustek 1975, Ford and Nelson 1978) may be used to modify the code without actually entering the EGS code itself. As a special feature to our simulation we also make use of the possibility of additional calls to AUSGAB --- ones other than the normal ones provided as default --- in order to extract the required information concerning the number of Compton interactions in the target. In the following paragraphs we describe the User Code called UCPISA, and the experimental apparatus that it simulates.

Figure 2 shows a schematic drawing of the experimental setup used at the CNR Institute of Clinical Physiology to perform Compton radiography. The unit is commonly known as the COSCAT prototype. A monoenergetic line source of gamma-rays, collimated to a narrow planar beam, irradiates a frontal section of a human thorax. A gamma camera equipped with a high resolution imaging collimator detects the Compton scattered radiation at 90° and produces an image of the section irradiated.

We have divided the simulation process into three steps: source simulation, target geometry, and scoring. Three different types of sources were considered (see Fig. 3): a "pencil" beam, a collimated point source, and a collimated line source. Source simulation is actually done in the MAIN program of UCPISA. The pencil beam is described by a Dirac delta function in position, size, and angle, and its implementation is trivial and will not be discussed further. The other two sources, on the other hand, are somewhat more difficult to sample due to the fact that the actual solid angle fraction subtended at the target by the source-collimator slit is often quite small (about 0.001), and normal rejection sampling techniques become very inefficient. Consequently, we had to derive sampling methods particular to the problem at hand, and these are described in detail in the Appendix. In this paper we have elected to present only the results obtained with the pencil beam and the collimated line source.

The source geometry we wish to simulate for the COSCAT prototype is illustrated in Fig. 4. A line source of ^{203}Hg gamma-rays (279 keV) having a length of 80 cm, and of negligible thickness, is placed in a parallelepiped box made out of lead; a variable slit (0.3 cm x 80 cm maximum), located 13.7 cm from the source, determines the length of the field and the solid angle subtended. Neither self-absorption in the source, nor scattering within the collimator, is considered. A simulation of the flux at the collimator exit plane is shown in Fig. 5 for a slit of 0.3 cm x 40 cm. Garbarino (1979) has measured the beam distribution of this device and has found it to be quite uniform (5%), in agreement with our simulation.

The second step in the simulation is to define the target geometry by means of subroutine HOWFAR. In all cases in this paper, we only consider a right parallelepiped, and the reader is referred to the EGS User Manual (Ford and Nelson 1978) for a description of how such a geometrical figure can be easily described in HOWFAR.

The third, and final, part of the simulation is the scoring, which is taken care of in subroutine AUSGAB. Photons which interact in and exit from the target are scored by outputting onto magnetic tape the various quantities of interest. For each photon history the following quantities are recorded: incident and exiting energies, coordinates and direction cosines corresponding to these photons, the number of Compton scatterings that the photon has undergone inside the phantom, and the angular details associated with each of these scatterings.

The combined program (EGS/UCPISA) is extremely fast as far as programs of this type are concerned. As many as 800 photons per second are generated and followed on the IBM-370/168; that is, it takes about 1.2 milliseconds per photon history, which is at least a factor of ten faster than the Battista and Bronskill (1978) program run on the same machine. This speed is due mostly to the fact that EGS makes use of in-line generation of functions (e.g., pseudo-random number generation), table lookup as opposed to function calls(e.g., for sine and cosine), and optimized sampling techniques. Furthermore, the code is very versatile, and is able to simulate much more complicated target geometries, such as those envisaged for an inhomogeneous phantom (the subject of a subsequent paper). Finally, virtually any electron-photon process can be scored and studied.

2.3 *Auxiliary Program for Subsequent Analysis*

Once the data produced by EGS/UCPISA has been written onto magnetic tape, an analysis program (EGSANAL) is used to histogram and plot the results of interest. We will not present the programming details of this code, but will merely describe the procedures that have been implemented in it. In the present case, the type of detector under investigation is a large-field gamma camera equipped with an imaging collimator that only accepts events around 90° to the phantom relative to the beam direction. It should be pointed out that a different type of detector arrangement will require only a different analysis program for the same source-target situation; that is, the Monte Carlo data output can (generally) be used again and again. We assume, as is typical in clinical applications, that the collimator (and detector) is flush with the phantom. In order to improve on the statistics during the Monte Carlo runs, two-plane symmetry is used for the pencil beam.

In actual cases in nuclear medicine, many types of imaging collimators are used, depending on such things as thickness, number of holes, packing fraction, sensitivity, etc. (Hine 1967). We limit ourselves to the geometric acceptance of the collimator without attempting to study edge/septum effects (this could be studied as well with EGS). Such effects have been studied by Jahns and Helmeke (1977). Therefore, the collimator that we simulate is an ideal device (efficiency = 1) in that all events are accepted provided that they are within the solid angle subtended by the holes making up the collimator. Since no packing fraction is introduced, the collimator as a whole can be thought of as a series of "virtual" cylindrical holes, each of which are centered on the exit point which the scattered photon makes with the phantom surface (see Fig. 6). The diameter of the virtual cylinders varies between 0.1 cm to infinity (i.e., no collimation whatsoever). The length of the cylinders is fixed at 5.0 cm.

In the discussion that follows, we refer to the various sizes of the virtual collimators as D_1, D_2, ...D_{25}, D_∞, where the number indicates the diameter (in millimeters). For each D-type collimator under study, we are able to present several histograms by using the information recorded for each photon. We can, for example, obtain the multiplicity distribution (number of Compton events) versus the scattered energy, the M/S ratio within a given energy window or at a particular depth, the spatial resolution for both S and M events, etc. Furthermore, the photopeak efficiency of the detector, as well as its energy and spatial resolution, can be folded-in in order to simulate the real situation as best as possible. We present comparative studies for several D-type virtual collimators and for three incident gamma energies in the next section.

3. Monte Carlo Results

In this section we present the results obtained from the EGS/UCPISA Monte Carlo calculation as analyzed by the auxiliary program EGSANAL. Two source geometries were considered: the pencil beam and the collimated line source. In the first case, three incident photon energies (100, 279, 500 keV) were chosen in order to cover the useful energy range in nuclear medicine imaging; namely, from below 140 keV (^{99m}Tc) up to almost 662 keV (^{127}Cs). As a midpoint energy we selected 279 keV, corresponding to the gamma-ray from ^{203}Hg. For the collimated line source case we only considered one energy (279 keV). In either situation the target was a 20 x 20 x 20 cm^3 water phantom, and the detector considered in the analysis program was a gamma camera having virtual cylindrical collimators of different diameters, as described in the previous section. The active region of the gamma camera was taken to be 20 cm x 20 cm in the analysis program, corresponding to the phantom surface itself.

3.1 *Pencil Beam Results*

Typical photon spectra for various Compton scattering multiplicities, n_c, are shown in Fig. 7 for an incident photon energy of 279 keV. A D_∞ -type collimator, corresponding to no collimation, and an energy window between 165 and 195 keV, was used to obtain Fig. 7a. As we see from this figure, the 90^o single scattering peak is spread out because the solid angle acceptance is large. Furthermore, the overall height of the double scattering histogram is of the same order of magnitude as the n_c = 1 case, and we can easily see that the higher order multiplicity photons will contribute significantly to the total scattering signal.

This is also reflected in Fig. 8a, where the multiplicity distribution, integrated over the energy window, is shown. As already pointed out by several authors, it is quite evident that a rather tight spatial collimation is required in order to reduce the M/S ratio to a significant level for clinical applications.

The corresponding plots for a D_3-type simulated collimator are shown in Figs. 7b and 8b. Such a collimator is representative of a typical imaging collimator used with conventional gamma cameras. We clearly see from the figures that the $n_c = 2$ contamination to the $n_c = 1$ signal drops by one order of magnitude, and the higher order scattering terms are even more depressed. By using information scored by the EGS/UCPISA code, we have attempted to find empirical correlations between the first and second order Compton scattering polar angles, such as $dN/d|\theta_1 \pm \theta_2|$, etc. To find such correlation functions might allow us to devise methods for speeding up the Monte Carlo program. Unfortunately, those that were found were also found to be dependent on the phantom depth in ways that were not suitable to parametrization (Bellazzini et al 1979).

In Fig. 9 we show typical calculated spectra for single and multiple scattering (solid and dashed histograms, respectively) for the three incident photon energies, and for three virtual collimators. The Monte Carlo calculation itself was terminated whenever a photon reached an energy corresponding to the Compton backscatter energy, $E'(180^{\circ})$, except for the 500 keV case, where a higher energy cutoff was used (see Table 1).

To simulate the actual experimental situation, the finite energy and spatial resolution of the gamma camera, as well as the detector efficiency, must be folded into the Monte Carlo data in a continuous way. In Table 1 we also present efficiency and resolution data for a typical NaI(Tl) gamma camera (Garbarino 1979).

In Fig. 10 we give the multiple to single scattering ratio, M/S, taking into account the resolution data from Table 1 and integrating over the respective energy windows. The solid lines were drawn through the points to guide the eye. The points labeled (d) represent, more or less, an ideal detector coupled to a D_3-type collimator. That is, a 1% energy window centered about $E'(90^o)$ was used, which represents the ultimate limit in terms of the M/S ratio that one could eventually afford by using a large matrix of Ge(Li) detectors (Strauss and Sherman 1979), apart from efficiency difficulties.

Figure 10 suggests a general 1/E dependence of M/S ratio with incident photon energy. This is quite understandable from the following argument. We first note that the multiple scattering is largely dominated by the $n_c = 2$ component. In the energy range considered, the Klein-Nishina cross section is roughly proportional to 1/E, so that the M contamination goes as $1/E^2$ and, hence, the M/S ratio is proportional to 1/E. From Fig. 10 it is also clear that M/S does not change appreciably from D_{10} to D_3 and will not decrease much more by further reducing the diameter of the collimator because of the finite energy resolution of the gamma camera. It is important to keep in mind, however, that any reduction of the collimator diameter will reduce quadratically (approximately) the sensitivity of the system, leading to an increase in the dose delivered to the phantom for the same number of detected photons. The spatial resolution of the collimator itself increases approximately linearly. A reasonable compromise, therefore, has to be found between sensitivity and spatial resolution; that is, between density resolution and position accuracy for a given dose. As we shall see in Section 4, the reasonable compromise which is chosen in actual cases is well simulated by a D_3-type collimator. The photon spatial distribution obtained using a D_3-type collimator with a typical NaI(Tl) gamma camera and a 279 keV source is shown in Fig. 11, where the solid and dashed histograms are for single and multiple scattering events, respectively. Finally, the spatial resolution for single scattering events is plotted in Fig. 12 as a function of the collimator diameter for a typical NaI(Tl) gamma camera and a 279 keV source.

As was stated previously, it is worthwhile to study the dependence of the M/S ratio on the target depth in order to derive simple correction algorithms that can be applied to clinical data. Figure 13 shows the single (solid) and multiple (dashed) scattering histograms versus target depth for a D_3-type collimator. Figures 13b, d, and f take into account the characteristics of the gamma camera (from Table 1); whereas, Figs. 13a, c, and e do not, and correspond to choosing a maximum energy window set by the source energy and the Monte Carlo cutoff (see Table 1). Solid lines have been drawn through the histograms in order to indicate trends. The exponential attenuation dependence of the single scatter component, as well as the Compton buildup of multiple scattering events, is clearly seen. The peak of the multiple scattering distribution is observed to move to higher depths as the source energy increases.

3.2 *Collimated Line Source Results*

A ^{203}Hg (279 keV) collimated line source (0.3 cm x 60 cm) was simulated as described in Section 2.2 and the Appendix. Essentially no differences were observed when these results were compared with those of the pencil beam presented in the previous section. This is demonstrated in Fig. 14 for D_3 and D_{10} collimators using typical gamma camera characteristics according to Table 1. Figs. 14a, c, and e correspond to the pencil beam case, and Figs. 14b, d, and f to the collimated line source. It should be noted that the spatial distribution, in the case of the collimated line source (see Fig. 14d), was calculated in the analysis program by evaluating the distance between the direction of the incident photon and the perpendicular to the detector plane measured from the point where the outgoing photon leaves the phantom.

Differences between the two sets of plots would naturally reflect the different conditions of irradiation. Apart from marginal edge effects at the sides of the phantom, which appear minor for a D_3-type collimator, the results are very similar for the pencil beam and collimated line source. Hence, it is reasonable to assume that for small collimator apertures (e.g., D_3-D_{10}), the M/S ratio as a function of incident energy remains essentially the same for the two source types.

In Fig. 15, the M/S ratio is plotted as a function of depth into the phantom for two collimator sizes (D_{10} = solid circles, D_3 = crosses). It is apparent, within the statistics indicated, that there is no difference between the two sets of data; hence, there is no evidence of dependence with collimator diameter in the range of small collimator apertures. On the same figure the ratio between double and single scattering, M_2/S, is plotted (open circles) for a D_{10}-type collimator. It is easy to prove that, in a simple approximation, one would expect M_2/S to depend linearly on the phantom depth, Z, and on the given transversal thickness of the phantom, D. The straight line shown in Fig. 15 is indeed a least-square fit to the M_2/S data using a parametrization of the form $C_1(Z+C_2D)$, with C_1 and C_2 constant. Further investigation of the dependence of M_2/S and M/S upon the transversal thickness will be presented in a subsequent paper.

4. Comparison of Monte Carlo Results and Experimental Data

As previously mentioned, Bellazzini et al (1978) have attempted to correct their experimental data for tomographic studies of the lung by accounting for the attenuation of the primary beam. A ^{203}Hg line source defined by a 0.3 cm x 60 cm slit (see Section 3.2) was used in the experiment. The target, which was located 10 cm from the exit plane of the slit, consisted of a box filled with wet sawdust having a density of 0.3 g/cm^3. The box was constructed out of 0.16 cm thick perspex with dimensions 16 cm x 16 cm x 10 cm (see insert to Fig. 16).

A large-field gamma camera (TOSHIBA Jumbo Camera - GCA 202) equipped with a medium-energy, high-resolution type collimator was located at right angles to the box in order to detect scattered photons. The digital output of the gamma camera was in the form of a 64 x 64 matrix with a pixel size of 0.5 cm x 0.5 cm. The experimental data, however, was limited to a 32 x 32 matrix located well inside the acceptance field of the camera. The number of counts for each pixel was averaged over the dimensions of the matrix parallel to the linear source and rebinned into 16 bins in order to reduce the statistical errors. The data thus obtained are presented as a function of phantom depth in Fig. 16 (solid circles).

The Monte Carlo simulation, normalized to the total number of counts between 2 and 14 cm, is shown as a histogram in Fig. 16. Both the energy and spatial resolution, as well as the detector efficiency, of the gamma camera were taken into account in the simulation. In accordance with the actual experimental situation, a D_3-type collimator (i.e., 0.3 cm diameter) was chosen for the Monte Carlo analysis. The statistical errors associated with each of the histogram bins is of the order of 10%.

It is apparent from Fig. 16 that the experimental data are as much as 30% higher than the Monte Carlo results for phantom depths less than 2 cm. This discrepancy can be attributed to the fact that the perspex itself was not included in the geometrical description of the Monte Carlo simulation. We can demonstrate this by estimating the number of counts that are added to the first histogram bin due to the 0.16 cm thick perspex. The 194 counts in the first 2 cm of sawdust (Fig. 16) results in 323 counts/g cm^{-2}. The 0.190 g cm^{-2} of perspex ($\rho = 1.19$ g cm^{-3}) then accounts for 61 additional counts for a total of 255 counts, as shown by the dashed histogram in Fig. 16. The net result is agreement between the (corrected) Monte Carlo calculation and experiment.

In order to better understand the effect of multiple scattering on the measured results, several corrections can be made to the experimental data. The data (solid circles) in Fig. 16 can be corrected for attenuation of the incident beam through the phantom using a scaling factor $\exp(\mu t)$, where

$$\mu t = (\mu/\rho)(\rho_p t_p + \rho_s t_s) , \qquad (2)$$

with μ/ρ = total mass attenuation coefficient ($cm^2\ g^{-1}$) in water at 279 keV,

ρ_p, ρ_s = density of perspex and sawdust (1.19 and 0.3 g cm^{-3}), respectively,

t_p, t_s = thickness (cm) of perspex and sawdust, respectively, traversed by the incident photons prior to reaching a given pixel.

The straight line a) in Fig. 16 was obtained from a least-square fit to the corrected data (open circles).

A second correction has been made by Bellazzini et al (1978) to the experimental data to account for the divergence of the photons from the source. The solid line b) shows the result of making this correction to line a). If no other effects are present, this final representation of the experimental data should give a constant value with depth into the phantom. As is clearly seen, there is an upward slope which we attribute to multiple scattering in the phantom. In order to understand this better, we have plotted the ratio of total to single scattering (histogram and right-hand scale) that was obtained from the Monte Carlo simulation of this problem. Apart from the region below 2 cm, which has been discussed above, the agreement is quite good.

A conclusion that can be made from the results that have been presented in Fig. 16 is that a positive bias as large as 25% will be introduced if corrections are only made for attenuation in the phantom and divergence from the source. In their experimental paper, Bellazzini et al (1978) have suggested that such a bias could be due to multiple scattering contamination. A similar trend, although in different experimental conditions (i.e., narrow beam geometry and small volume target), has also been observed by Kennett and Webber (1976), Huddleston and Bhaduri (1979), and Huddleston, Bhaduri and Weaver (1979), all of whom suggest the same explanation.

5. Conclusions

In this paper, we have extensively investigated the multiple scattering contamination in 90° Compton scattering radiography for homogeneous media as a function of the incident photon energy for several source and detector geometries. For a 20 x 20 x 20 cm^3 phantom, when a gamma camera equipped with a conventional imaging collimator is simulated as a detector, such a contamination may be of the same order of magnitude as the 90° single scatter signal. The M/S ratio goes approximately as 1/E and is rather independent of the collimator diameter (in the 3 to 10 mm range). An ultimate limit of about 7% for M/S may be reached only when a high resolution detector (e.g., Ge(Li)) is used. Nonetheless, M/S may be predicted and corrected for, with an accuracy of about 5% (e.g., see Fig. 16). For phantom dimensions less than a photon mean-free path --- that is, about 8 g cm^{-2} for a biological target and an incident photon energy of 279 keV --- the multiple scattering contamination is dominated by the double scattering events. In this case, a linear parametrization of M/S with phantom depth can be used to remove the bias introduced by multiple scattering in order to obtain "quasi multiple scattering free" results.

Finally, the use of the EGS code as applied to this problem (EGS/UCPISA) has greatly reduced the computer time limitations previously seen. EGS, with appropriately designed User Codes, might have some application in similar problems, such as single photon tomography or positron tomography.

Acknowledgments

It is a pleasure to acknowledge the Director of the INFN Sezione di Pisa, Professor A. Stefanini, for his interest and continuous support in this work. We would also like to thank Drs. A. Herz and K. Goebel of the HS Division at CERN where this work was initiated. We appreciate the effort made by T. M. Jenkins and Dr. R. C. McCall of the Radiation Physics Group at SLAC for reviewing the manuscript, as well as for the hospitality shown one of us (A.D.G.) during a recent short stay at SLAC. The technical skill of E. Carboni (Pisa) in drawing the figures, and of Mrs. G. Manzerra (Pisa) and Mrs. R. Parker (SLAC) in carefully typing the manuscript, is also acknowledged.

Appendix

Sampling of a Point Source through a Rectangular Slit

Figure A.1a shows a schematic drawing of the geometry for the sampling of an isotropic point source on the central axis of a rectangular slit. In this figure, the source is located at the origin of a Cartesian coordinate system whose z-axis lies along the major dimension, ℓ_o, of the slit and the y-axis is perpendicular to the slit plane. The minor dimension of the slit is Δx and the slit plane is located a distance d from the source.

The solid angle fraction subtended by the slit, $\Delta\Omega_o/4\pi$, is about 0.005, so that the rejection technique has a very low efficiency for a point isotropic source. In terms of saving computer time, a more favorable sampling consists of forcing all photons through the slit and extracting the direction of each under the restriction that the distribution is uniform inside the solid angle

$$\Delta\Omega_o = \int_{\theta_1}^{\theta_2} \int_{\phi_1}^{\phi_2} \sin\theta \, d\theta d\phi \quad , \tag{A.1}$$

where θ_1 and θ_2 are the limiting polar angles and ϕ_1 and ϕ_2 are the limiting azimuthal angles in a polar coordinate system centered at S. In most situations, θ and ϕ are correlated; however, for a rectangular slit in the xz-plane, it is easy to show that they may be treated independently under the approximation of neglecting second-order terms, or higher, in $\Delta x/2$. In our simulation, $\Delta x/2$ is always less than 0.03, so that

$$\Delta\Omega_o = \int_{\phi_1}^{\phi_2} d\phi \int_{\cos\theta_1}^{\cos\theta_2} [-d(\cos\theta)] \quad , \tag{A.2}$$

where ϕ_1 and ϕ_2 apply for all θ, and θ_1 and θ_2 apply for all ϕ (see Figs. A.1b and A.1c).

The direction of a photon which passes through point P can be obtained from

$$R_\phi = \int_{\phi_1}^{\phi} d\phi \Bigg/ \int_{\phi_1}^{\phi_2} d\phi \ ,$$

$$R_\theta = \int_{\cos\theta_1}^{\cos\theta} [-d(\cos\theta)] \Bigg/ \int_{\cos\theta_1}^{\cos\theta_2} [-d(\cos\theta)] \ , \tag{A.3}$$

where R_ϕ and R_θ are two random numbers extracted under a flat distribution in the interval (0,1). Integrating, we obtain

$$\phi = -\frac{\Delta\phi_o}{2} + \Delta\phi_o R_\phi \ ,$$

$$\cos\theta = \cos\theta_1 + \left(\cos\theta_2 - \cos\theta_1\right) R_\theta \ , \tag{A.4}$$

where

$$\frac{\Delta\phi_o}{2} = \frac{\phi_2 - \phi_1}{2} = \tan^{-1}(\Delta x/2d) \ .$$

From Fig. A.1c,

$$\theta_1 = \frac{\pi}{2} + \alpha_1 \ ,$$

$$\theta_2 = \frac{\pi}{2} + \alpha_2 \tag{A.5}$$

where the convention is that positive angles are measured counterclockwise (e.g., $\alpha_1 < 0$ in Fig. A.1c). Even though the source is located at the origin of the coordinate system in Figs. A.1, for generality we will now give it a position along the z-axis, z_s, and obtain

$$\begin{aligned} \tan\alpha_1 &= \left(z_s - \ell_o/2\right)/d \quad , \\ \tan\alpha_2 &= \left(z_s + \ell_o/2\right)/d \quad , \end{aligned} \tag{A.6}$$

where a careful examination will verify that the signs are consistent with Fig. A.1c and the angle convention. Hence,

$$\begin{aligned} \cos\theta_1 &= -\sin\alpha_1 = -\frac{\left(z_s - \ell_o/2\right)/d}{\sqrt{1 + \left[\left(z_s - \ell_o/2\right)/d\right]^2}} \\ \cos\theta_2 &= -\sin\alpha_2 = -\frac{\left(z_s + \ell_o/2\right)/d}{\sqrt{1 + \left[\left(z_s + \ell_o/2\right)/d\right]^2}} \quad . \end{aligned} \tag{A.7}$$

The histograms in Figs. A.2a through f give the results obtained with the above sampling technique applied to the following geometry: $d = 13.7$ cm, $\ell_o = 40.0$ cm, $\Delta x = 0.3$ cm. Figure A.2a shows a typical distribution of photons along the x-axis at the slit and Fig. A.2b gives the same distribution as a function of ϕ in degrees. Figure A.2c shows a typical distribution along the z-axis and Fig. A.2d gives the same distribution as a function of $\cos\theta$. Finally, Figs. A.2e and f give the photon distribution as a function of the direction cosines for the x- and y-axis, respectively. After normalizing to $\Delta\Omega_o/4\pi$ and to the total number of particles sampled, the results shown in Figs. A.2 were compared to those obtained by the rejection technique and excellent agreement was found.

Once ϕ and $\cos\theta$ have been sampled, the direction cosines can be calculated from

$$
\begin{aligned}
u &= \sin\theta \cos\phi \quad , \\
v &= \sin\theta \sin\phi \quad , \\
w &= \cos\theta \quad .
\end{aligned}
\tag{A.8}
$$

In order to match the coordinate system used in the EGS Monte Carlo program (see Fig. A.3), we must translate a distance d along the y-axis and perform a double rotation of the coordinate system. The direction cosines in the EGS coordinate system (primes) are then given in terms of the extracted ϕ and θ by

$$
\begin{aligned}
u' &= \cos\theta \quad , \\
v' &= \sin\theta \cos\phi \quad , \\
w' &= \sin\theta \sin\phi \quad .
\end{aligned}
\tag{A.9}
$$

It should be pointed out that it is much more difficult to sample directly in the prime coordinate system because $\cos\theta'$ and ϕ' must be extracted under a joint distribution function. In addition to being analytically complicated, the steepness of the function, itself, creates sampling problems. Hence, the reason for choosing the scheme that we have adopted.

Sampling of a Line Source through a Rectangular Slit

Since equations (A.7) are general and valid for any z_s, we now wish to extend the above ideas to a line source of length Δz (see Fig. 4). This is accomplished most easily by first extracting $|z|$ on the interval $(0, \Delta z/2)$, and then determining the sign of z on a 50/50 basis.

To extract $|z|$, we must perform a weighted sampling for the solid angle subtended by each point z of the half-source; namely,

$$R_z = \int_0^z f(z)\,dz \Bigg/ \int_0^{\Delta z/2} f(z)\,dz \quad , \tag{A.10}$$

where R_z is a random number sampled uniformly on the interval (0,1), and where f(z) is given according to previous considerations by

$$f(z) = \Delta\Omega(z) = \left[\cos\theta_2(z) - \cos\theta_1(z)\right] \left[\phi_2(z) - \phi_1(z)\right] \quad . \tag{A.11}$$

Using equations (A.7), and making use of the fact that ϕ_2 and ϕ_1 do not depend on z (e.g., see Fig. A.1b), we obtain

$$R_z = \frac{1}{\alpha}\left[\sqrt{d^2 + \left(z + \ell_o/2\right)^2} - \sqrt{d^2 + \left(z - \ell_o/2\right)^2}\right] \quad , \tag{A.12}$$

where α is a normalization factor given by

$$\alpha = \sqrt{d^2 + \left(\Delta z + \ell_o\right)^2/4} - \sqrt{d^2 + \left(\Delta z - \ell_o\right)^2/4} \quad . \tag{A.13}$$

Inverting equation (A.12) and taking into account the fact that z must be positive, we get

$$|z| = r\left[1 + 4d^2\Big/\left(\ell_o^2 - 4r^2\right)\right]^{\frac{1}{2}} \quad , \tag{A.14}$$

where $r = R_z\alpha/2$ and α is given by equation (A.13). The final selection of z on the interval $(-\Delta z/2,\ \Delta z/2)$ is then given by

$$z = |z|\left(2\,R_{sign} - 1\right) \quad , \tag{A.15}$$

where R_{sign} is a random number, again chosen uniformly on the interval (0,1). Figure A.4 shows the distribution of extracted events along the z-axis, at the source, for a source length of 80 cm and the same slit used to obtain the results (see Fig. A.2) for the collimated point source.

Once z has been determined, $\cos\theta$ and ϕ are obtained in the same manner as described above for sampling a point source [i.e., equations (A.4) and (A.7)].

References

Battista, J. J., Santon, L. W., and Bronskill, J. J., 1977, Phys. Med. Biol., 22, 229-244.

Battista, J. J., and Bronskill, M. J., 1978, Phys. Med. Biol., 23, 1-23.

Bellazzini, R., Del Guerra, A., Krachmalnicoff, A., Neri, F., Tonelli, G., Garbarino, M., Guzzardi, R., and Mey, M., 1978, in "Proceedings of the International Conference on Computerized Tomography: Related Instrumentation and Data Processing Techniques," Pavia, Italy, October 9-10, 1978, 137-147.

Bellazzini, R., Del Guerra, A., Tonelli, G., Venturi, R., and Nelson, W. R., 1979, LXV Congress of the Italian Physics Society, Ancona, Italy, October 4-9, 1979, SIF Bulletin, 117, 32.

Clarke, R. L., 1965, Chalk River, Ontario, Canada, A.E.C.R. 2270.

Clarke, R. L., and Van Dyk, G., 1969, in Medical Radioisotope Scintigraphy, STl/PUB/193 (Vienna: IAEA), Vol. I, 247-260.

Clarke, R. L., and Van Dyk, G., 1973, Phys. Med. Biol., 18, 532-539.

Cook, A. J., and Shustek, L. J., 1975, Stanford Linear Accelerator Center Computation Research Group Report, CGTM 165.

Dohring, K., Reiss, K., and Fabel, H., 1974, Pheumonologie, 150, 345-359.

Endo, M., Matsumoto, T., Iinuma, T. A., and Tateno, Y., 1979, Jpn. J. Nucl. Med., 16, 175-181.

Farmer, F. J., and Collins, M. P., 1971, Phys. Med. Biol., 16, 577-586.

Farmer, F. J., and Collins, M. P., 1974, Phys. Med. Biol., 19, 808-818.

Ford, R. L., and Nelson, W. R., 1978, Stanford Linear Accelerator Center, SLAC-210.

Garnet, E. S., Kennett, T. J., Kenyon, D. B., and Webber, C. E., 1973, Radiology, 106, 209-212.

Garbarino, M., 1979, University of Pisa, Istituto di Fisica, Corso di Cultura in Fisica Sanitaria, PhD Thesis, unpublished.

Geise, R. A., and McCullough, E. C., 1977, Radiology, 124, 133-141.

Giuntini, C., Guzzardi, R., Pistolesi, M., Mey, M., and Solfanelli, S., 1979, in "Proceedings of the International Titisee Conference", Titisee, October 19-21, 1978, Prog. Resp. Res., 11, 76-85.

Guzzardi, R., Mey, M., Pistolesi, M., Solfanelli, S., Giuntini, C., 1977, J. Nucl. Med. All. Sci., 21, 72.

Guzzardi, R., Mey, M., Pistolesi, M., Solfanelli, S., Giuntini, C., 1978, J. Nucl. Med. All. Sci., 22, 11-19.

Guzzardi, R., 1980, private communication.

Hazan, G., Leichter, I., Loewinger, E., Weinreb, A., and Robin, G. C., 1977, Phys. Med. Biol., 22, 1073-1084.

Hine, G. J., editor, 1967, Instrumentation in Nuclear Medicine, Vol. I, Academic Press, New York.

Huddleston, A. L., and Bhaduri, D., 1979, Phys. Med. Biol., 24, 310-318.

Huddleston, A. L., Bhaduri, D., and Weaver, J., 1979, Med. Phys., 6, 519-522.

Jahns, E. G. H., and Helmeke, H. J., 1977, in "Proceedings of the International Symposium on Medical Radionuclide Imaging," Los Angeles, 1976 (Vienna: IAEA), Vol. I, 207-218 (IAEA-SM-210/102).

Kaufman, L., Gamsu, G., Savoca, C., Swann, S., Murphey, T., Hruska, B., and Palmer, D., 1976, IEEE Trans. Nucl. Sci., NS-23, 594-605.

Kelcz, F., Joseph, P. M., and Hilal, S. K., 1979, Med. Phys., 6, 418-425.

Kennett, T. J., and Webber, C. E., 1976, Phys. Med. Biol., 21, 770-780.

Lale, P. G., 1959, Phys. Med. Biol., 4, 159-166.

Lale, P. G., 1968, Radiology, 90, 510-517.

Leunbach, I., 1977, in "Proceedings of the International Symposium on Medical Radionuclide Imaging," Los Angeles, 1976 (Vienna: IAEA), Vol. I, 263-268 (IAEA-SM-210/158).

Mirell, S. G., Anderson, G. W., and Blahd, W. H., 1977, in "Proceedings of the International Symposium on Medical Radionuclide Imaging," Los Angeles, 1976 (Vienna: IAEA), Vol. I, 225-262 (IAEA-SM-210/70).

Nelson, W. R., and Jenkins, T. M., editors, 1980, Computer Techniques in Radiation Transport and Dosimetry, Plenum Press, New York.

Pistolesi, M., Solfanelli, S., Guzzardi, R., Mey, M., and Giuntini, C., 1977, J. Nucl. Med. All. Sci., 21, 79.

Pistolesi, M., Solfanelli, S., Guzzardi, R., Mey, M., and Giuntini, C., 1978, J. Nucl. Med., 19, 94-97.

Reiss, K., Ing, D., and Schuster, W., 1972, Radiology, 102, 613-617.

Rutherford, R. A., Pullan, B. R., and Isherwood, I., 1976a, Neuroradiology, 11, 15.

Rutherford, R. A., Pullan, B. R., and Isherwood, I., 1976b, Neuroradiology, 11, 23.

Sontag, M. R., Battista, J. J., Bronskill, M. J., and Cunningham, J. R., 1977, Radiology, 124, 143-149.

Strauss, M. G., and Sherman, I. S., 1979, Phys. Med. Biol., 1979, 24, 702-710.

Talbert, A. J., Brooks, R. A., and Morgenthaler, D. G., 1980, Phys. Med. Biol., 25, 261-269.

Webber, C. E., and Kennett, T. J., 1976, Phys. Med. Biol., 21, 760-769.

Zelefsky, M. M., and Schulz, R. J., 1968, Radiology, 91, 1208-1213.

Table 1. Kinematics and typical performance of the gamma camera.

Incident energy (keV)	100.0	279.0	500.0
E'(90^o) (keV)	83.6	180.5	252.7
Backscatter energy (keV)	71.9	133.4	169.0
Energy cutoff used in the Monte Carlo calculation	71.9	133.4	220.0
Photopeak efficiency at E'(90^o)	1.00	0.83	0.60
ΔE/E (FWHM) at E'(90^o)	0.142	0.111	0.102
Spatial resolution (FWHM) at E'(90^o) (mm)	7.33	5.36	4.88
Energy window setting about E'(90^o) (keV)	75-90	165-195	235-270

Figure Captions

1. Flow control with user using EGS.
2. Schematic drawing of the COSCAT apparatus.
3. Simulated source geometries: a) "pencil" beam, b) collimated point source, c) collimated line source.
4. Perspective drawing of the collimated line source: a) side view, b) top view.
5. Photon distribution along the z-axis at the collimator exit plane. The distribution is normalized to its mean value to show the uniformity in photon flux.
6. a) Coordinate system used in EGS/UCPISA: b) examples of "virtual" collimator simulation: the scattered photon γ' enters virtual collimator D_{25} and is accepted; photon γ'' is outside D_{25}.
7. Typical photon spectra for various Compton multiplicities for an incident photon energy of 279 keV: a) D_∞ collimator, b) D_3 collimator.
8. Compton scattering multiplicity distribution integrated over the energy window 165-195 keV for an incident photon energy of 279 keV: a) D_∞ collimator, b) D_3 collimator (statistics for each bin are indicated).
9. Typical spectra for single and multiple scattered photons (solid and dashed histograms, respectively) for the three incident photon energies (100, 279, 500 keV): a)-c) = D_∞ collimator, d)-f) = D_{10} collimator, g)-i) = D_3 collimator.
10. Multiple to single scattering ratio as a function of incident photon energy for three collimators. Curves a) through c) include the resolution of the gamma camera. Curve d) is for an "ideal" detector (see text).

11. Spatial distribution for a 279 keV source and a D_3 collimator: single scattering (solid histogram), multiple scattering (dashed histogram).

12. Spatial resolution (i.e., rms width) associated with single scattering distribution as a function of virtual collimator diameter for a 279 keV source.

13. Single and multiple scattering distributions (solid and dashed histograms, respectively) as a function of depth into the phantom for a D_3 collimator and for three incident energies: a),c),e) = maximum energy window, b),d),f) = actual gamma camera (see text).

14. Comparison between typical "pencil" beam and collimated line source results: a) and b) are energy spectra histograms for single (solid) and multiple (dashed) scattering. c) and d) are spatial distributions for single (solid) and multiple (dashed) scattering. e) and f) plot the multiple to single scattering ratio as a function of depth into the phantom.

15. Multiple to single scattering ratio as a function of depth into the phantom for a 279 keV collimated line source: D_{10} collimator (solid circles), D_3 collimator (crosses). Also shown (open circles): double to single scattering ratio for a D_{10} collimator with a least-square straight line fit (see text).

16. Comparison of Monte Carlo results with experimental data (see text).

A.1 Schematic drawing of the geometry for the sampling of a point source positioned on the symmetry axis of a rectangular slit: a) perspective view, b) side view, c) top view.

A.2 Typical photon distributions at the slit plane: a) versus x, b) versus y, c) versus z, d) versus w (z-direction cosine), e) versus u (x-direction cosine), f) versus v (y-direction cosine).

A.3 Sampling coordinate system (x,y,z) and its relation to the EGS coordinate system (x',y',z') as used in this problem (UCPISA).

A.4 Typical distribution, at the line source, for sampling along the z-direction with the rectangular slit as a constraint (see text).

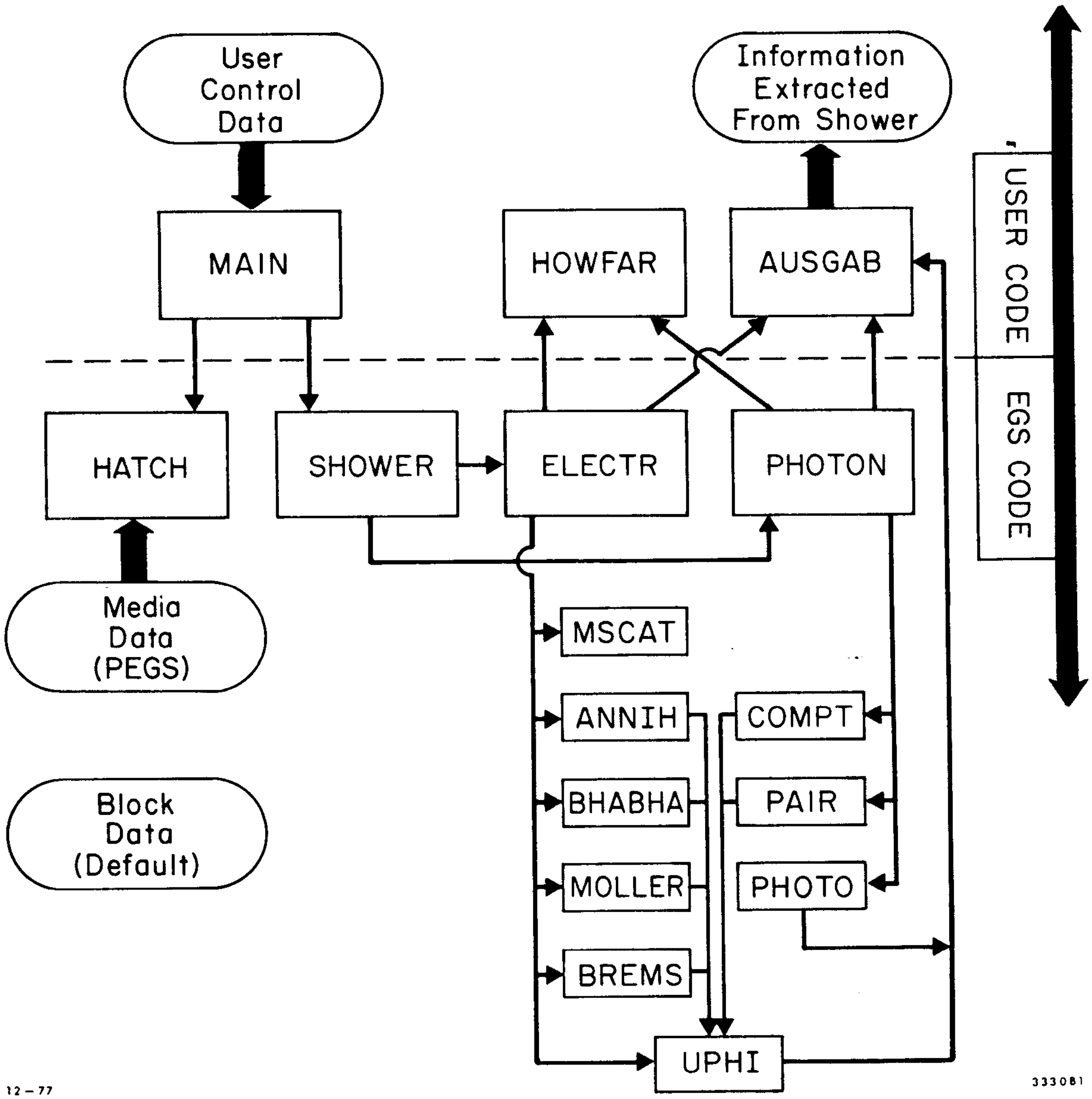
User Control Data
Information Extracted From Shower
MAIN
HOWFAR
AUSGAB
USER CODE
EGS CODE
HATCH
SHOWER
ELECTR
PHOTON
Media Data (PEGS)
MSCAT
ANNIH
COMPT
Block Data (Default)
BHABHA
PAIR
MOLLER
PHOTO
BREMS
UPHI
12-77
333081

Fig. 1

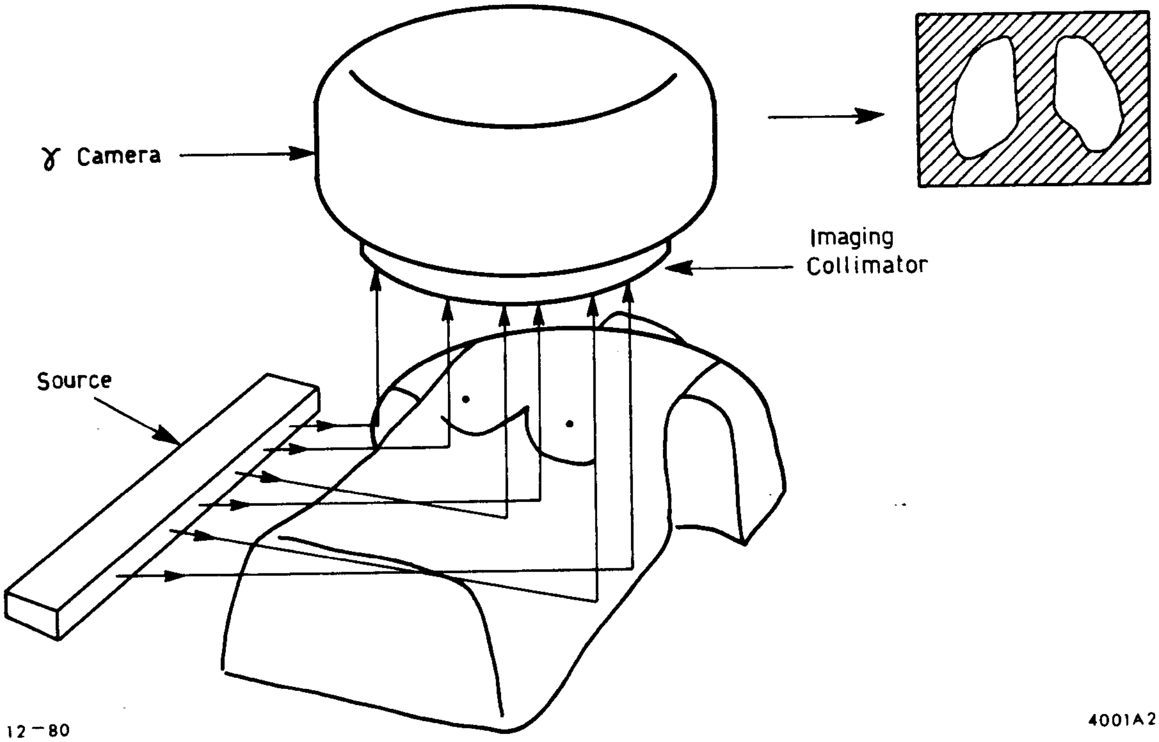

Fig. 2

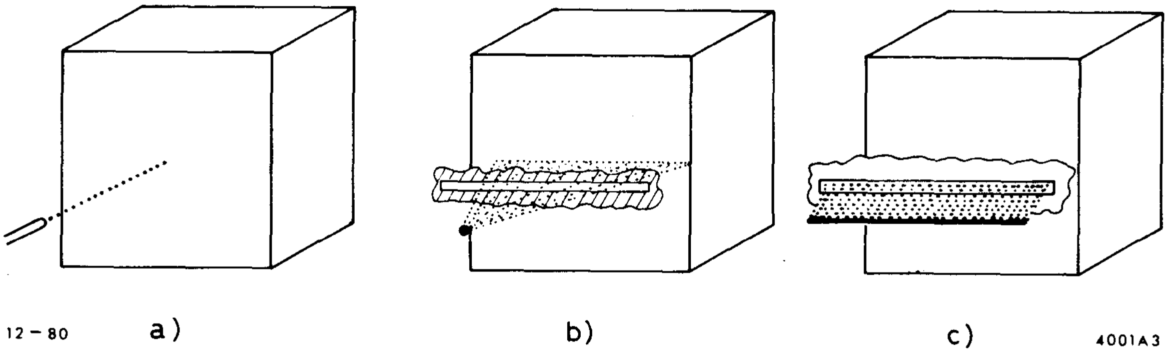

Fig. 3

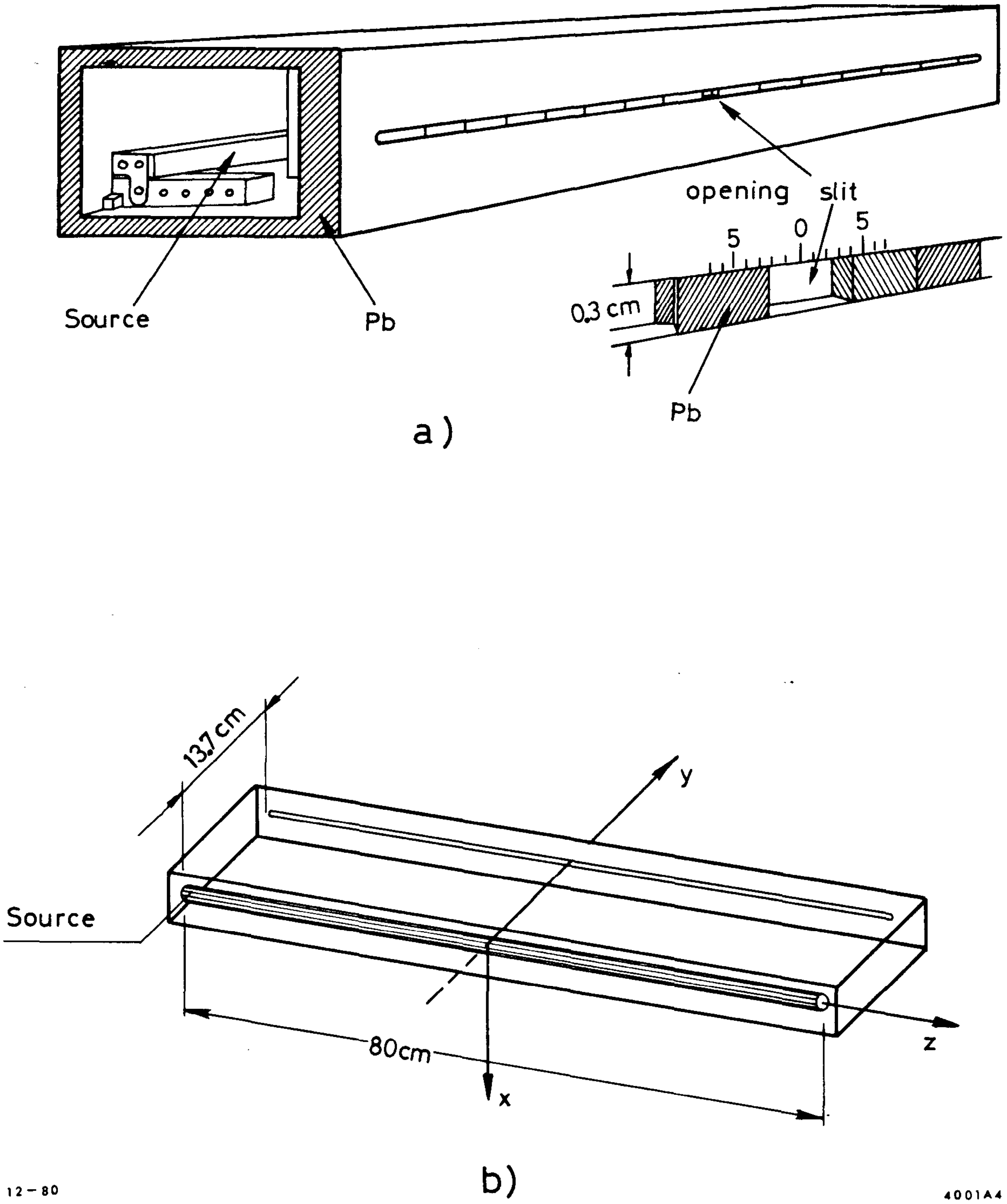
opening
slit
5
0
5
0.3 cm
Source
Pb
Pb
a)
13.7 cm
y
Source
z
80cm
x
b)
12-80
4001A4

Fig. 4

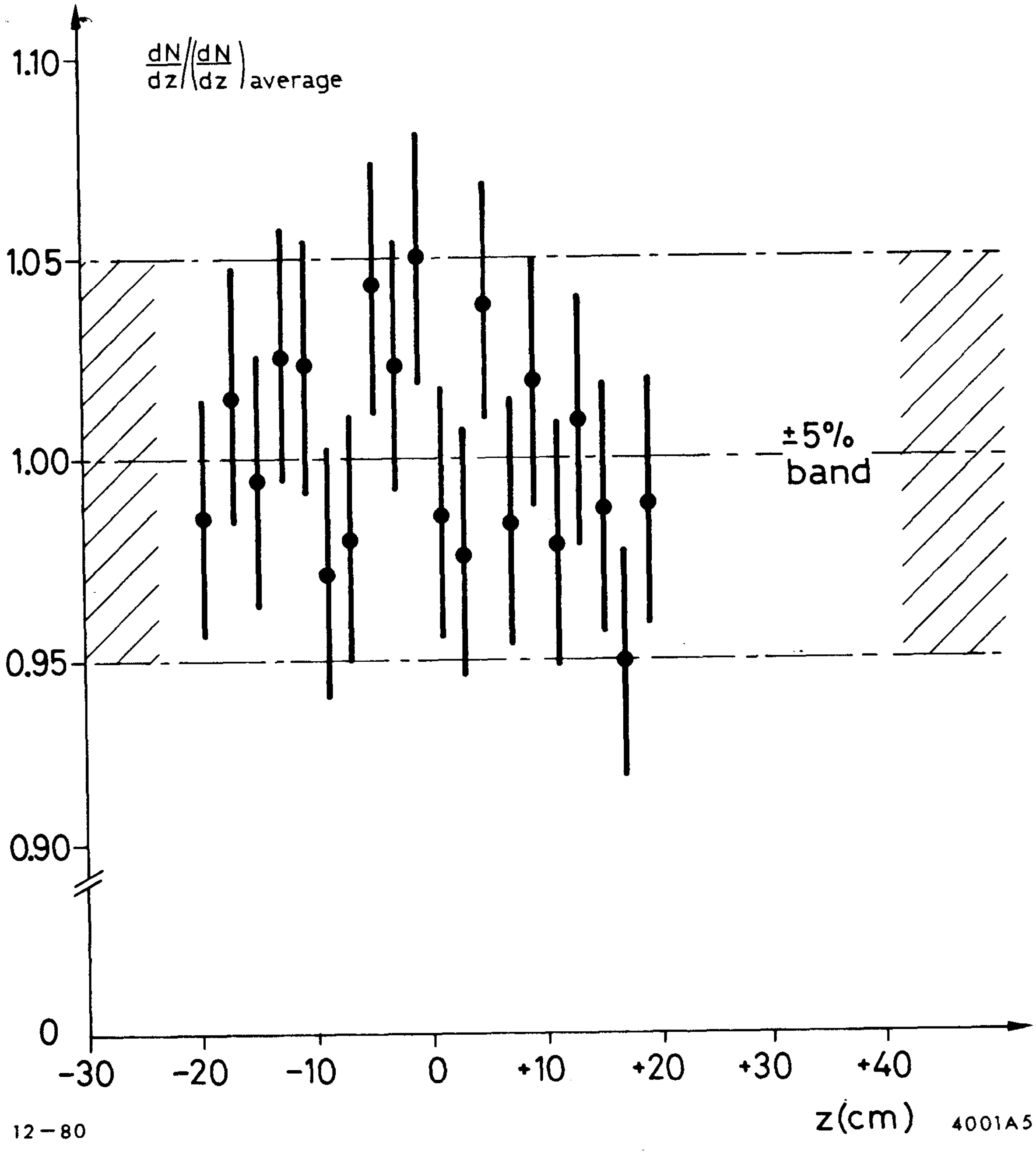

1.10
1.05
1.00
0.95
0.90
0
$\frac{dN}{dz} / \left(\frac{dN}{dz}\right)_{average}$
±5% band
-30
-20
-10
0
+10
+20
+30
+40
z(cm)
12-80
4001A5

Fig. 5

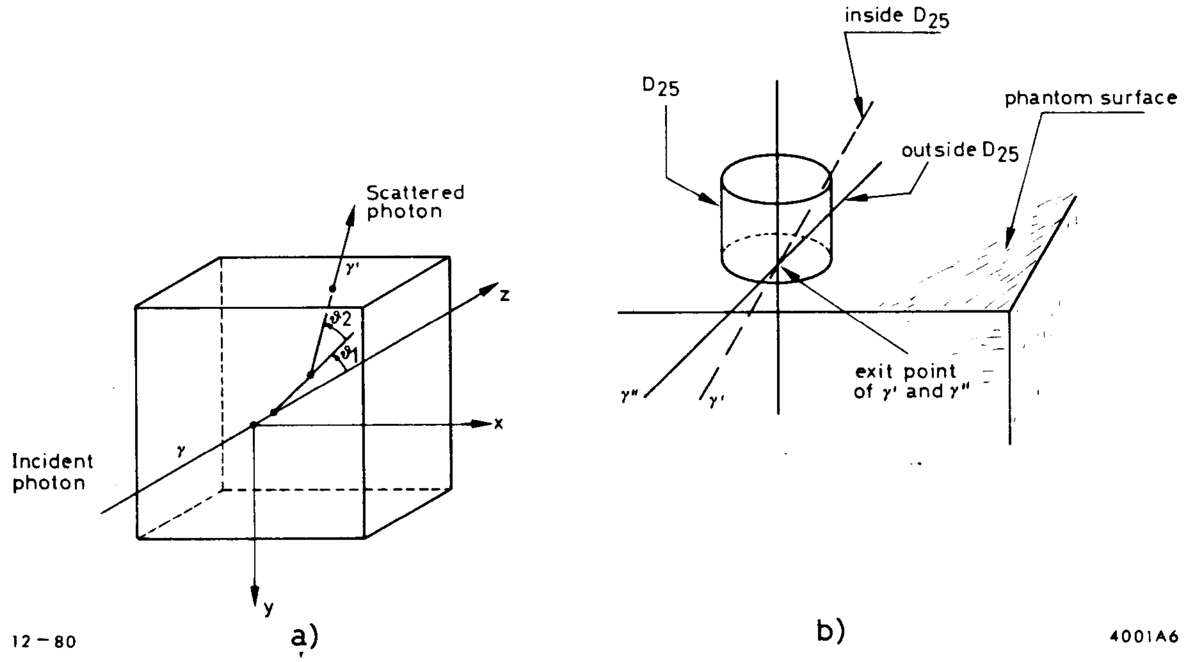
Scattered photon
γ'
ϑ_2
ϑ_1
z
x
y
γ
Incident photon
12-80
a)
inside D_{25}
D_{25}
phantom surface
outside D_{25}
γ''
γ'
exit point of γ' and γ''
b)
4001A6

Fig. 6

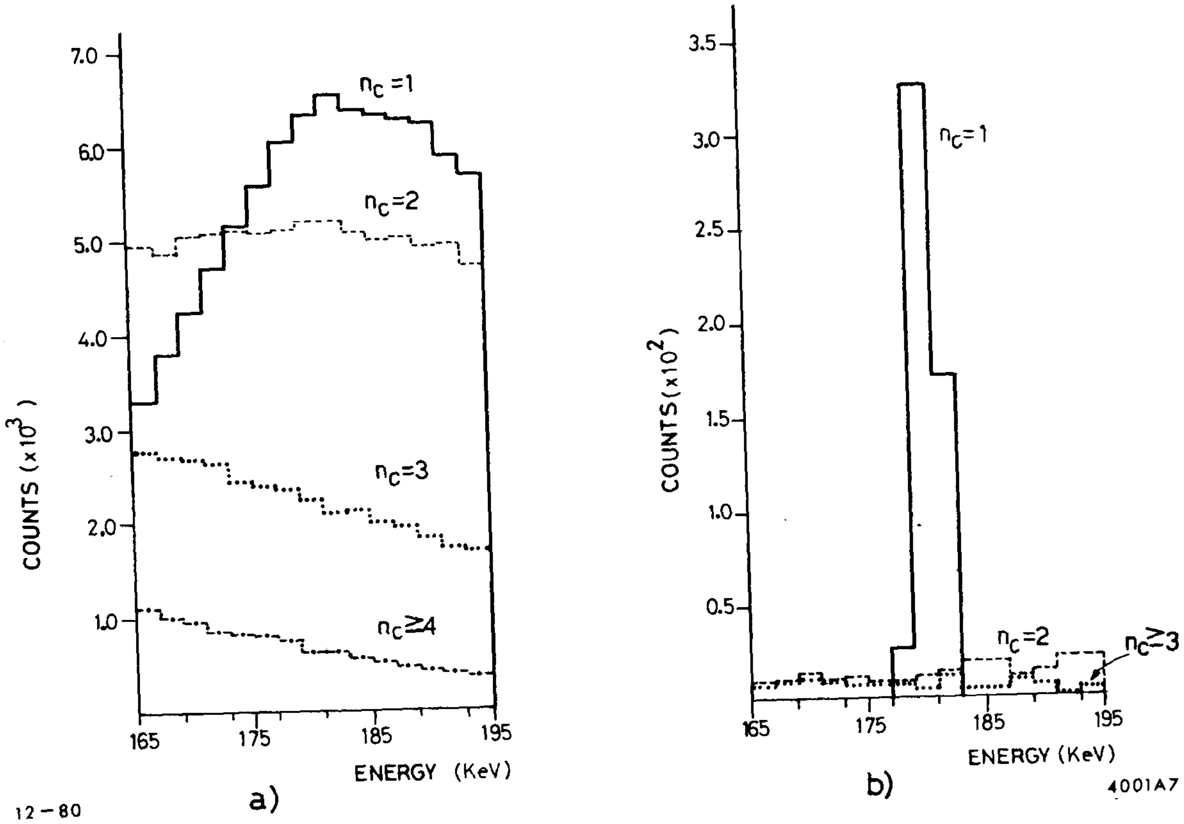
7.0
6.0
5.0
4.0
3.0
2.0
1.0
COUNTS (x10^3)
n_c =1
n_c=2
n_c=3
n_c≥4
165
175
185
195
ENERGY (KeV)
a)
12-80
3.5
3.0
2.5
2.0
1.5
1.0
0.5
COUNTS (x10^2)
n_c=1
n_c=2
n_c≥3
165
175
185
195
ENERGY (KeV)
b)
4001A7

Fig. 7

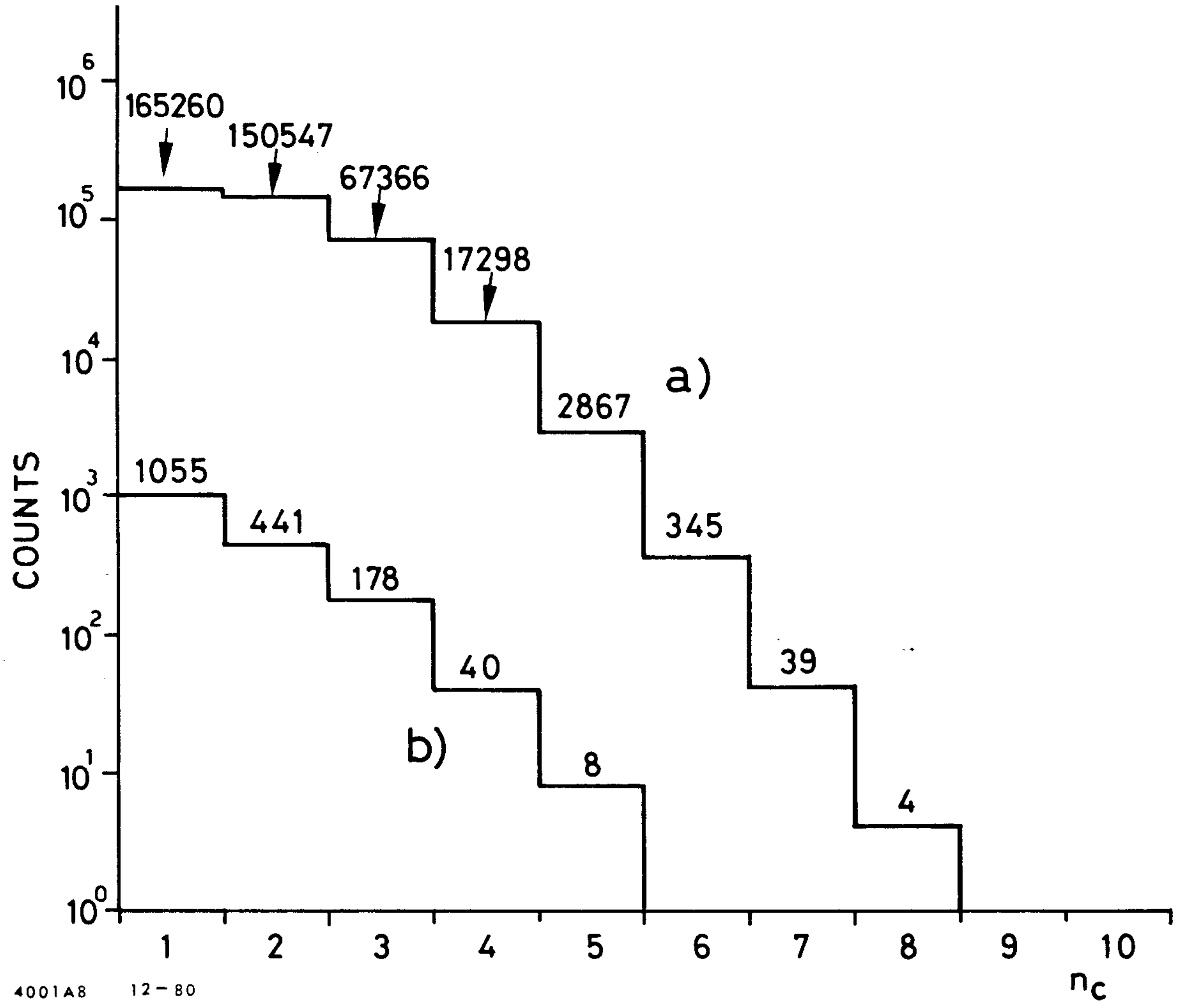

COUNTS
10^6
10^5
10^4
10^3
10^2
10^1
10^0
165260
150547
67366
17298
2867
345
39
4
a)
1055
441
178
40
8
b)
1
2
3
4
5
6
7
8
9
10
n_c
4001A8 12-80

Fig. 8

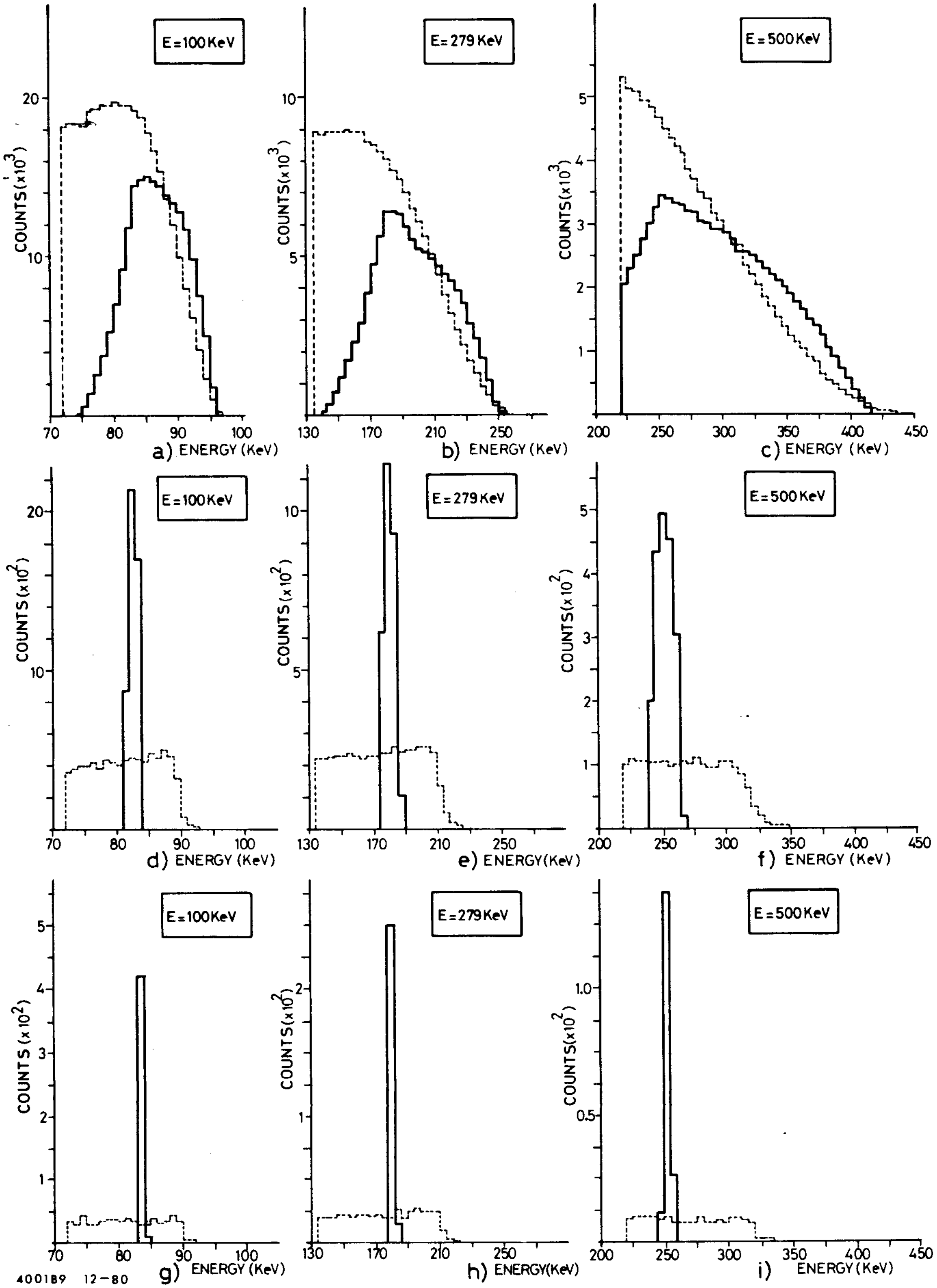
E=100KeV
E=279KeV
E=500KeV
COUNTS(x10^3)
COUNTS(x10^2)
20
10
5
4
3
2
1
1.0
0.5
70
80
90
100
130
170
210
250
200
300
350
400
450
a) ENERGY (KeV)
b) ENERGY (KeV)
c) ENERGY (KeV)
d) ENERGY (KeV)
e) ENERGY(KeV)
f) ENERGY (KeV)
g) ENERGY (KeV)
h) ENERGY(KeV)
i) ENERGY (KeV)
400189 12-80

Fig. 9

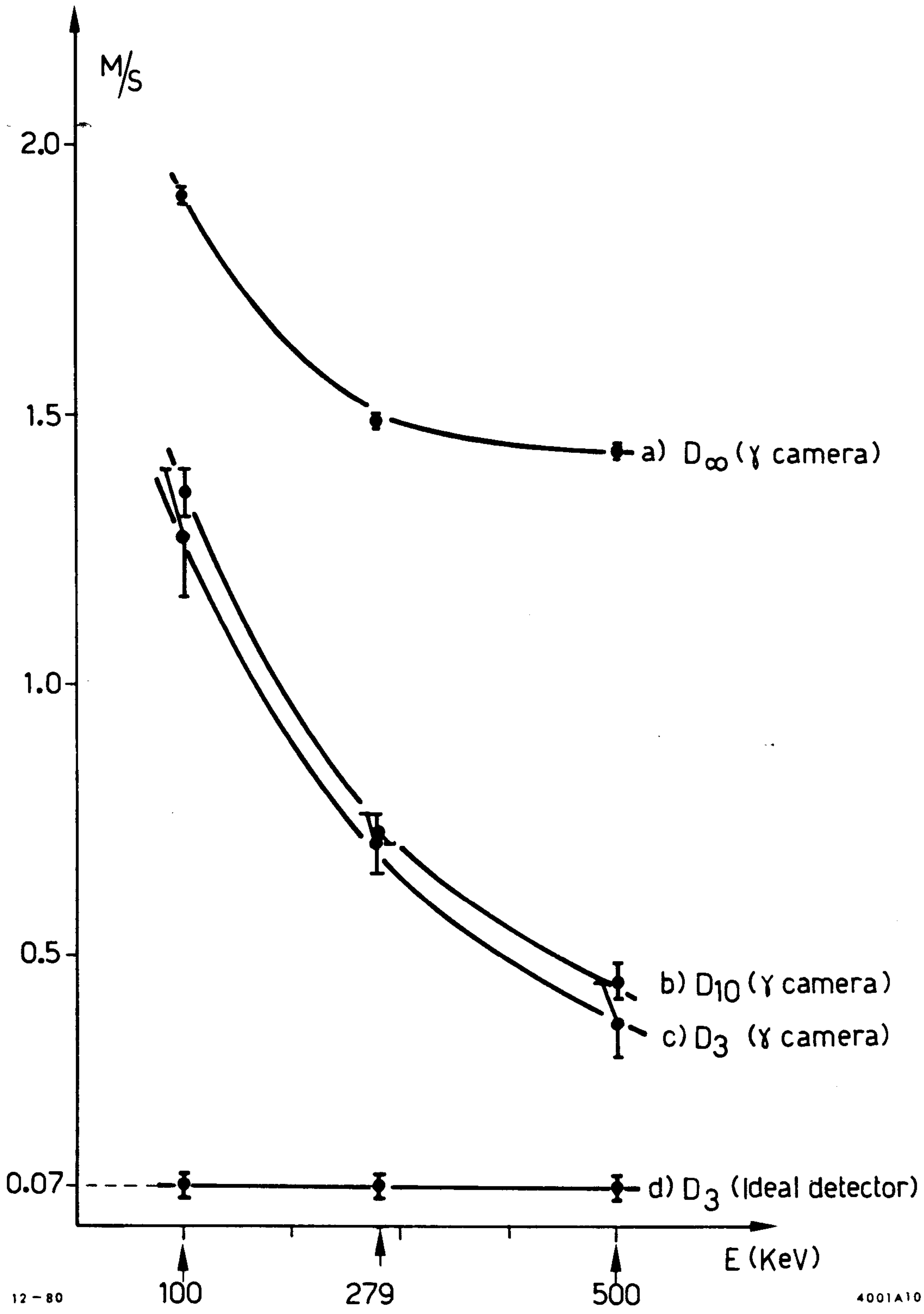
M/S
2.0
1.5
1.0
0.5
0.07
a) D_∞ (γ camera)
b) D_{10} (γ camera)
c) D_3 (γ camera)
d) D_3 (ideal detector)
E (KeV)
100
279
500
12-80
4001A10

Fig. 10

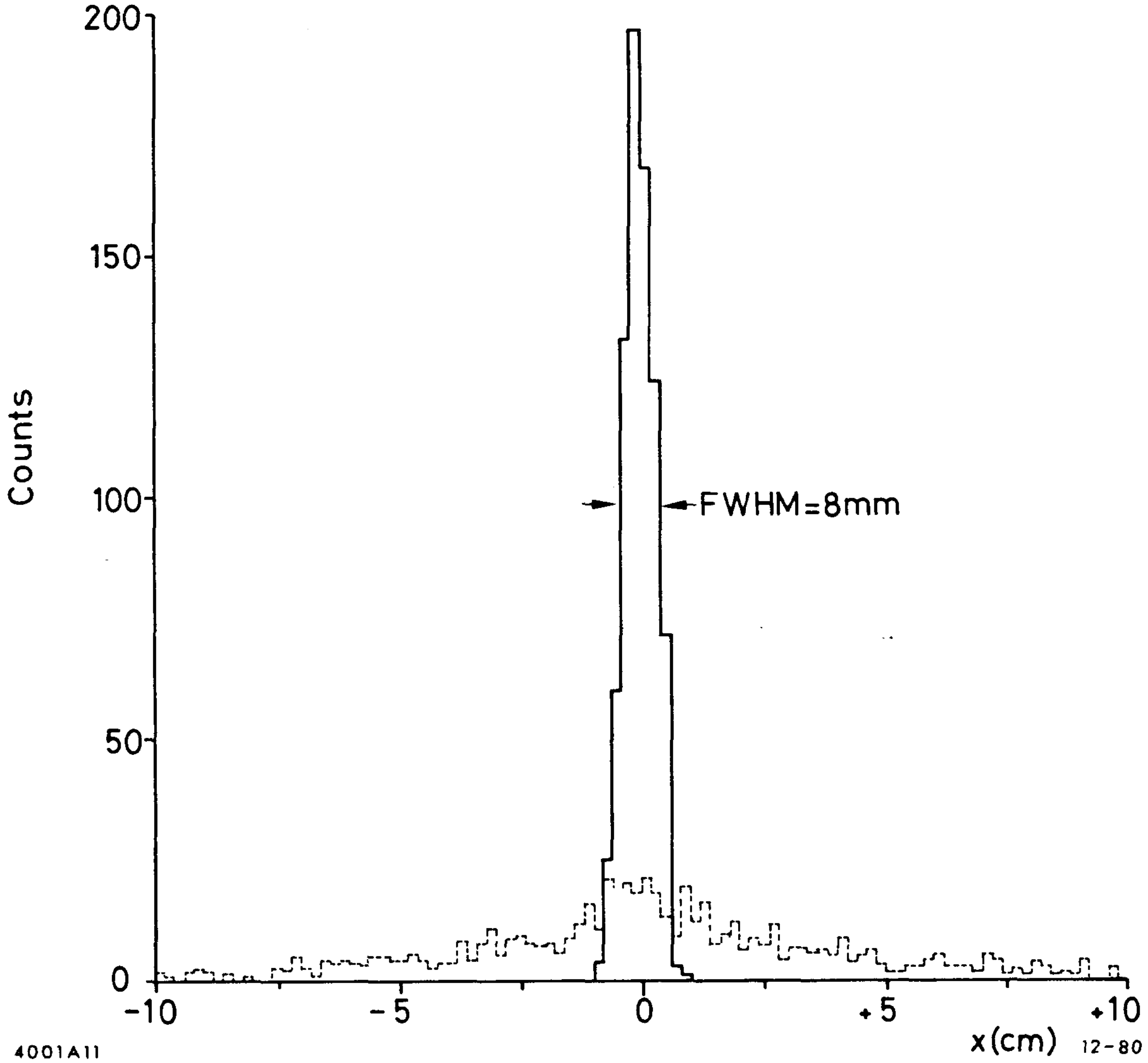

Fig. 11

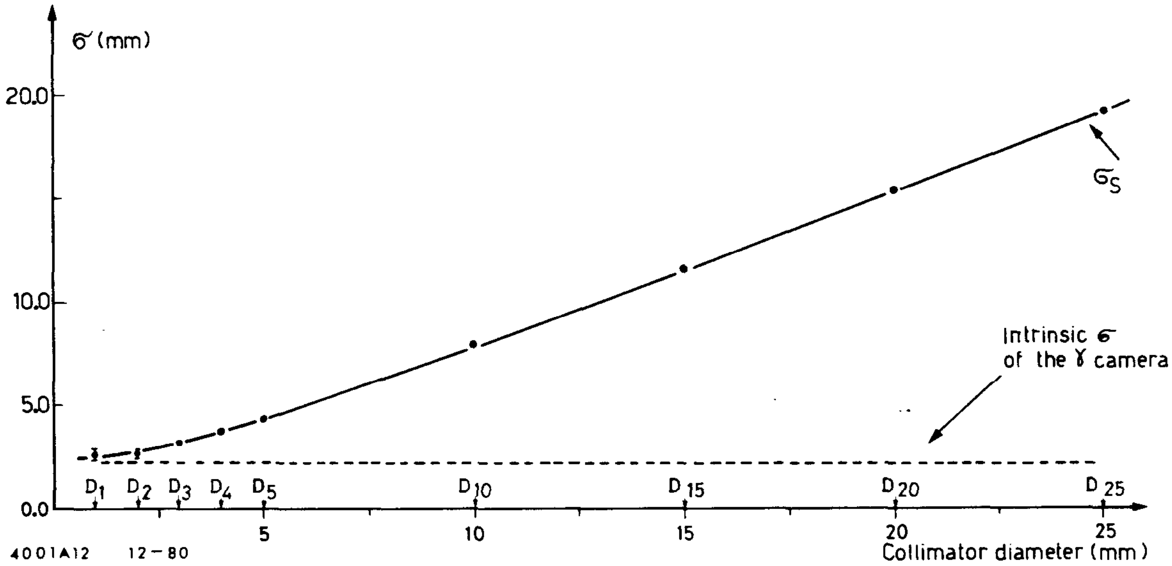
σ (mm)
20.0
10.0
5.0
0.0
σS
Intrinsic σ
of the γ camera
D1
D2
D3
D4
D5
D10
D15
D20
D25
5
10
15
20
25
Collimator diameter (mm)
4001A12
12-80

Fig. 12

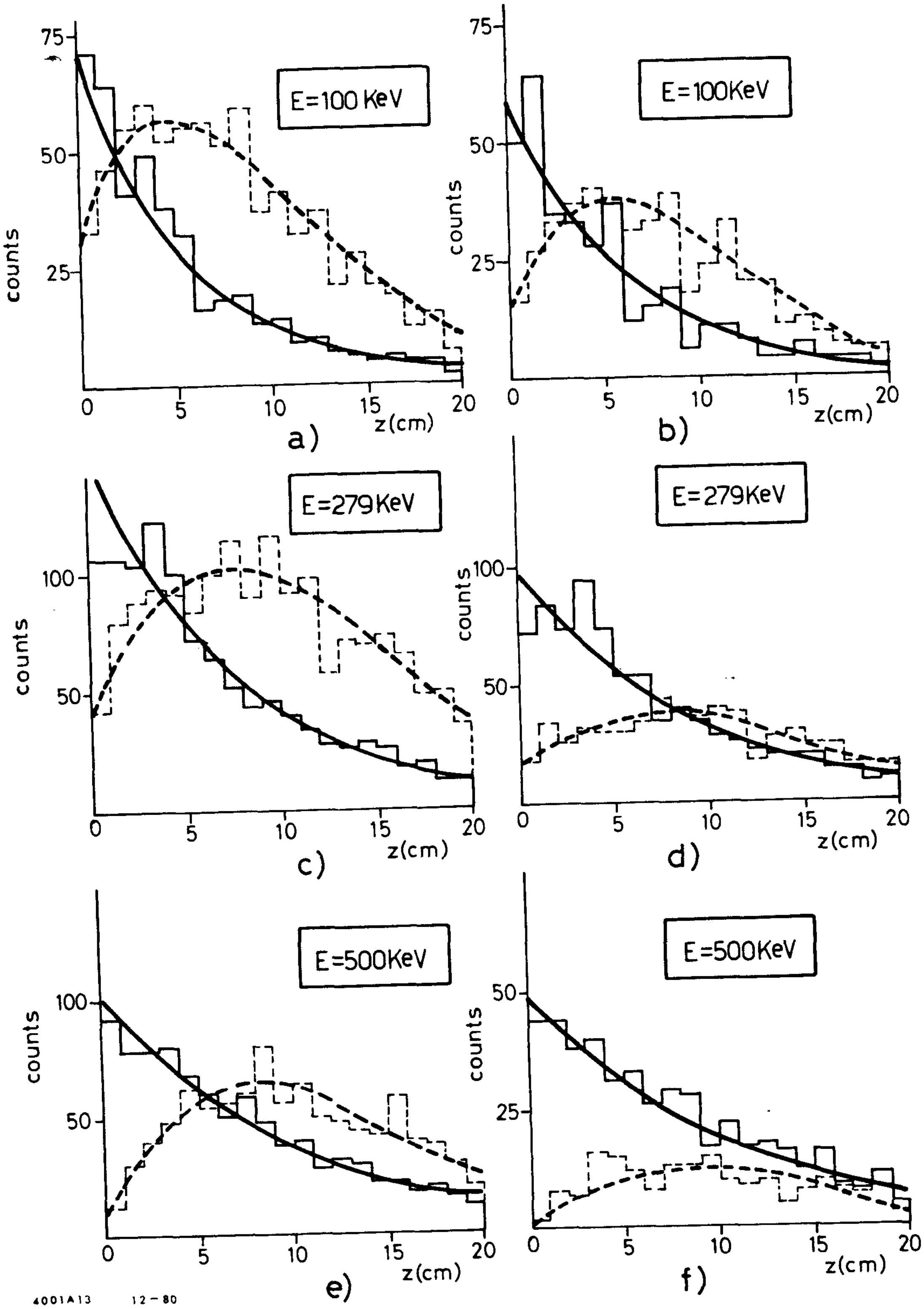
E=100 KeV
counts
75
50
25
0
5
10
15
20
z(cm)
a)
E=100KeV
counts
75
50
25
0
5
10
15
20
z(cm)
b)
E=279KeV
counts
100
50
0
5
10
15
20
z(cm)
c)
E=279KeV
counts
100
50
0
5
10
15
20
z(cm)
d)
E=500KeV
counts
100
50
0
5
10
15
20
z(cm)
e)
E=500KeV
counts
50
25
0
5
10
15
20
z(cm)
f)
4001A13 12-80

Fig. 13

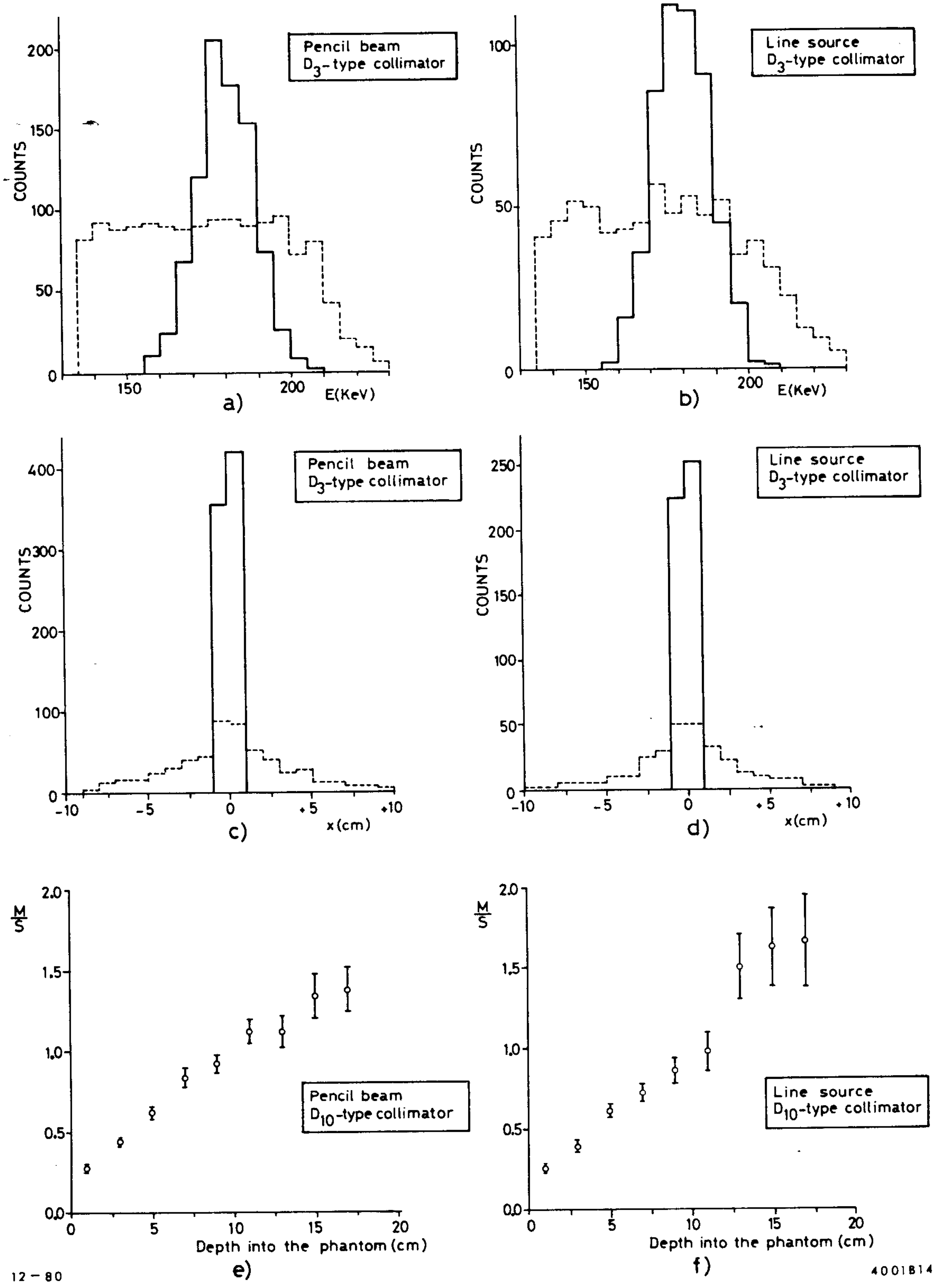
Pencil beam
D3-type collimator
COUNTS
0
50
100
150
200
150
200
E(KeV)
a)
Line source
D3-type collimator
COUNTS
0
50
100
150
200
E(KeV)
b)
Pencil beam
D3-type collimator
COUNTS
0
100
200
300
400
-10
-5
0
+5
+10
x(cm)
c)
Line source
D3-type collimator
COUNTS
0
50
100
150
200
250
-10
-5
0
+5
+10
x(cm)
d)
M/S
0.0
0.5
1.0
1.5
2.0
0
5
10
15
20
Depth into the phantom (cm)
Pencil beam
D10-type collimator
e)
M/S
0.0
0.5
1.0
1.5
2.0
0
5
10
15
20
Depth into the phantom (cm)
Line source
D10-type collimator
f)
12-80
4001B14

Fig. 14

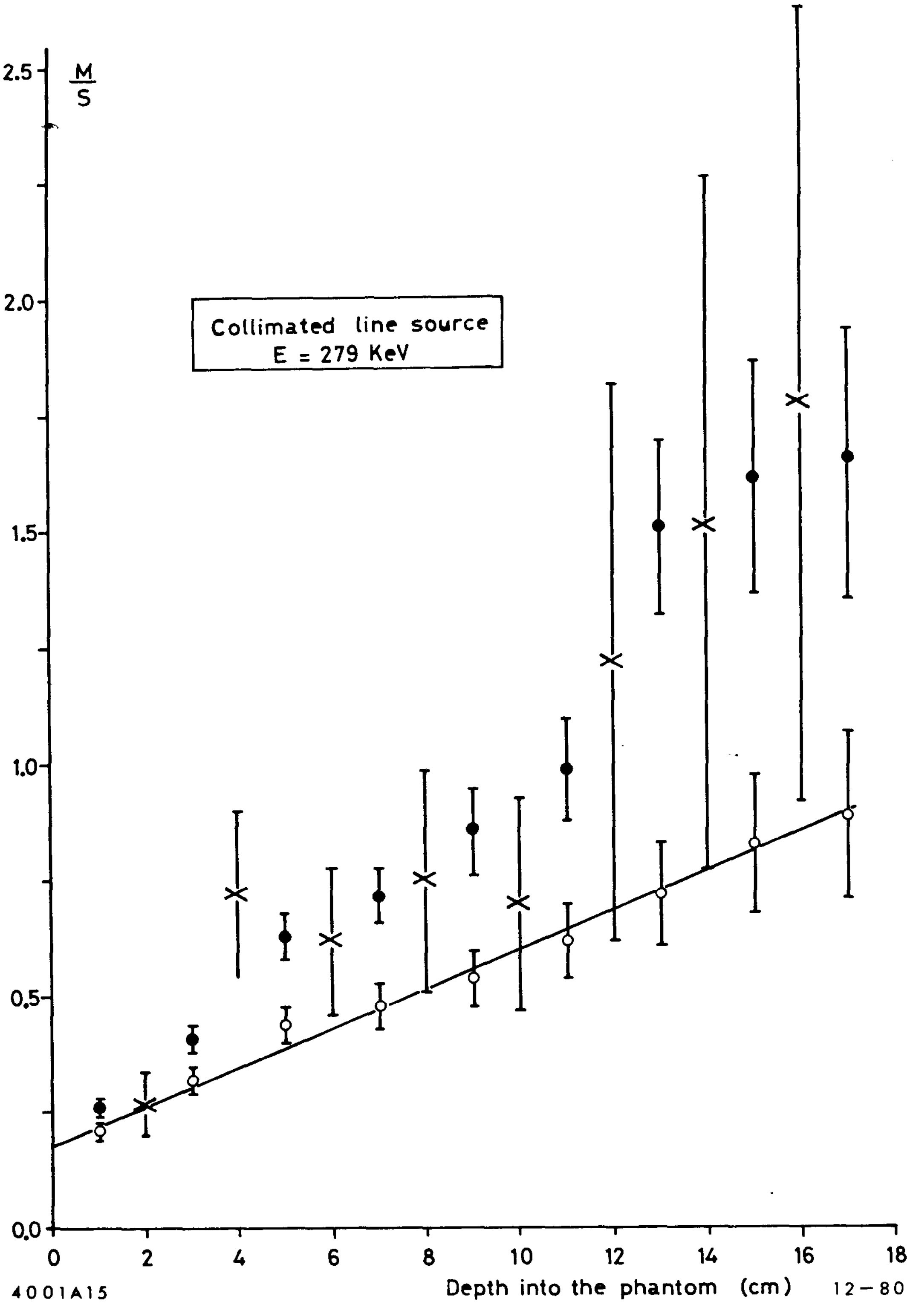

2.5
2.0
1.5
1.0
0.5
0.0
M/S
Collimated line source
E = 279 KeV
0
2
4
6
8
10
12
14
16
18
Depth into the phantom (cm)
4001A15
12-80

Fig. 15

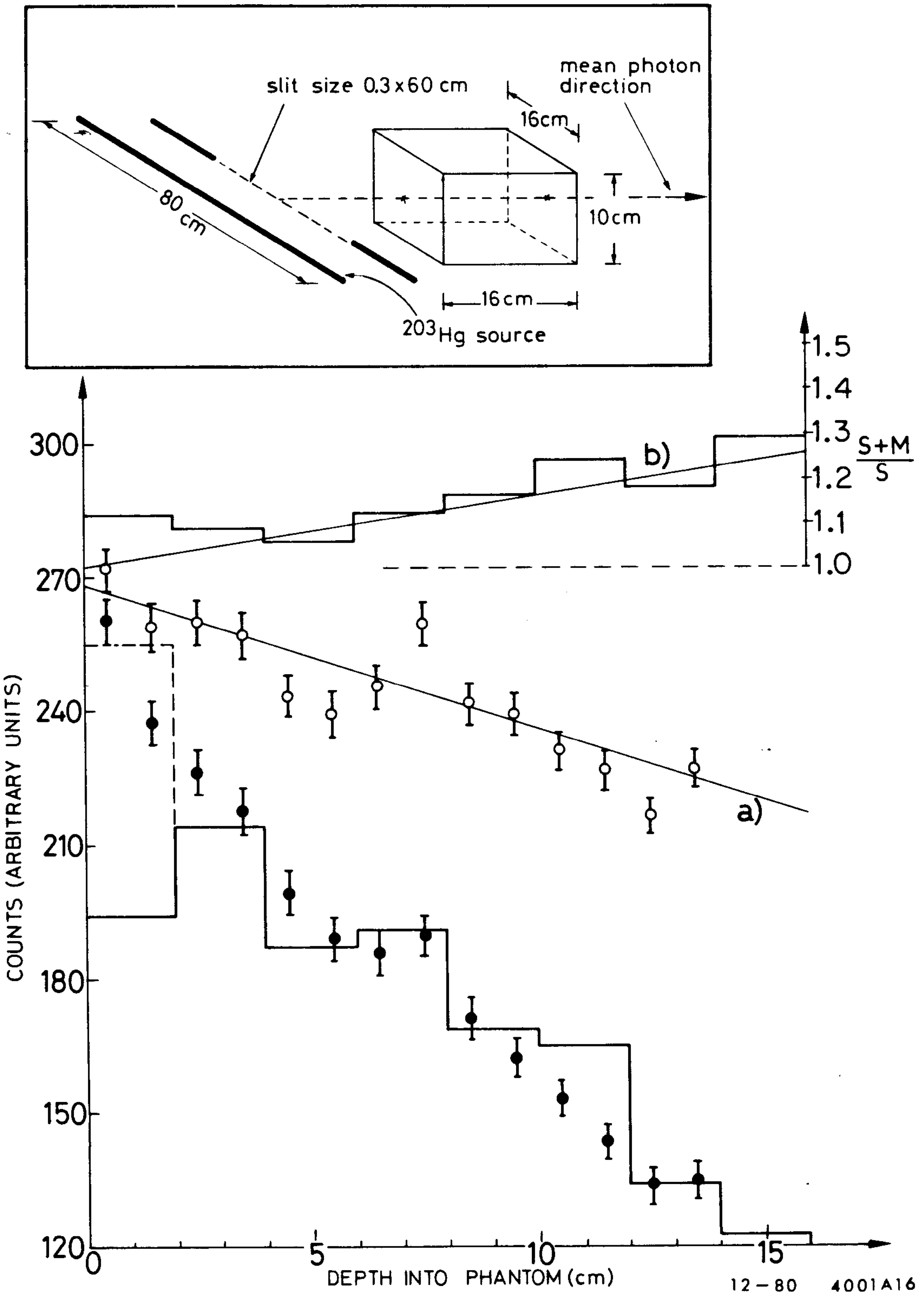

slit size 0.3x60 cm
mean photon direction
16cm
80 cm
10cm
16cm
203Hg source
1.5
1.4
1.3
1.2
1.1
1.0
S+M / S
b)
a)
300
270
240
210
180
150
120
COUNTS (ARBITRARY UNITS)
0
5
10
15
DEPTH INTO PHANTOM (cm)
12-80
4001A16

Fig. 16

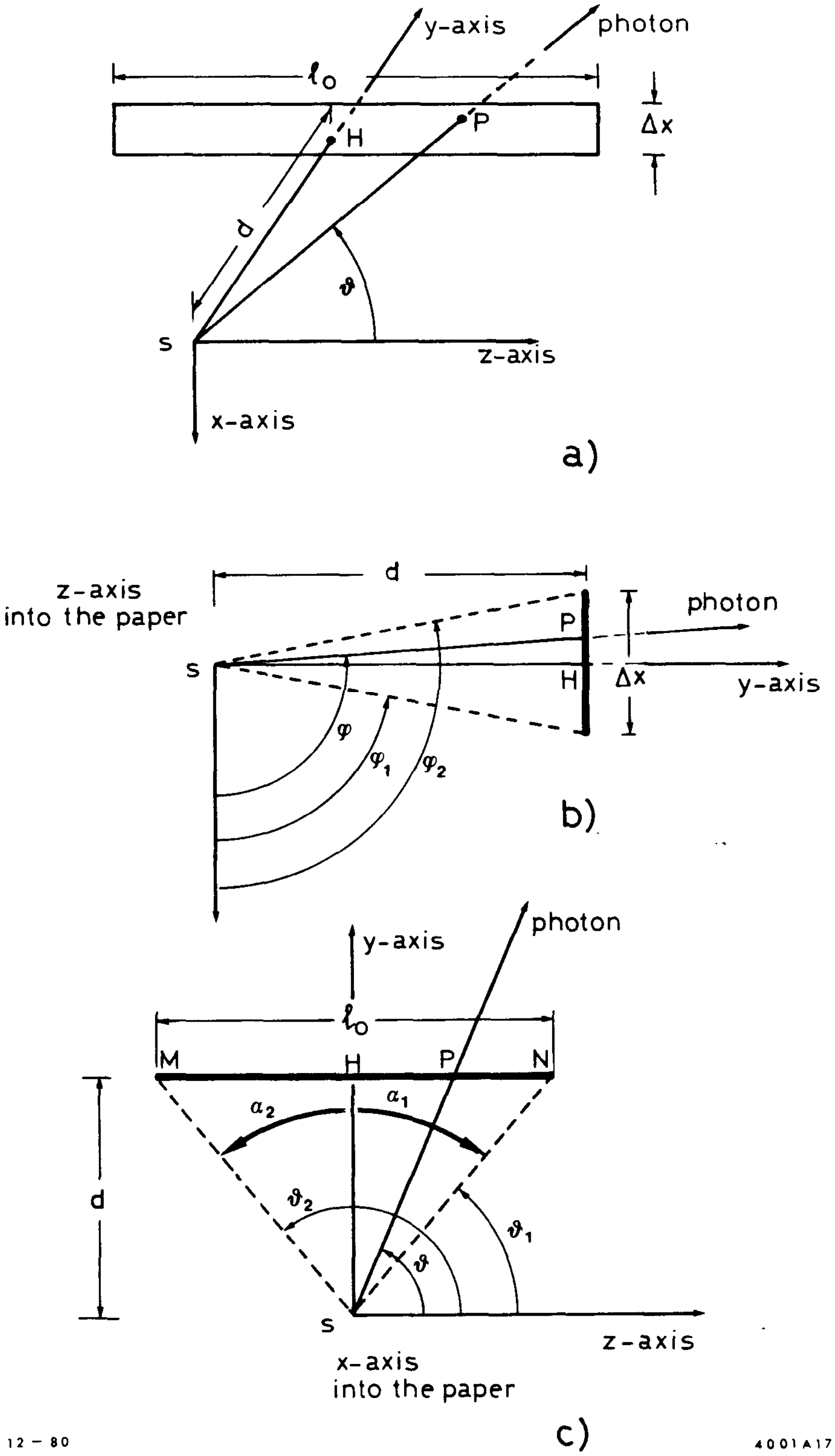
y-axis
photon
l_o
Δx
H
P
d
ϑ
s
z-axis
x-axis
a)
d
z-axis
into the paper
photon
P
s
H
Δx
y-axis
φ
φ_1
φ_2
b)
y-axis
photon
l_o
M
H
P
N
α_2
α_1
d
ϑ_2
ϑ_1
ϑ
s
z-axis
x-axis
into the paper
12 – 80
c)
4001A17

Fig. A.1

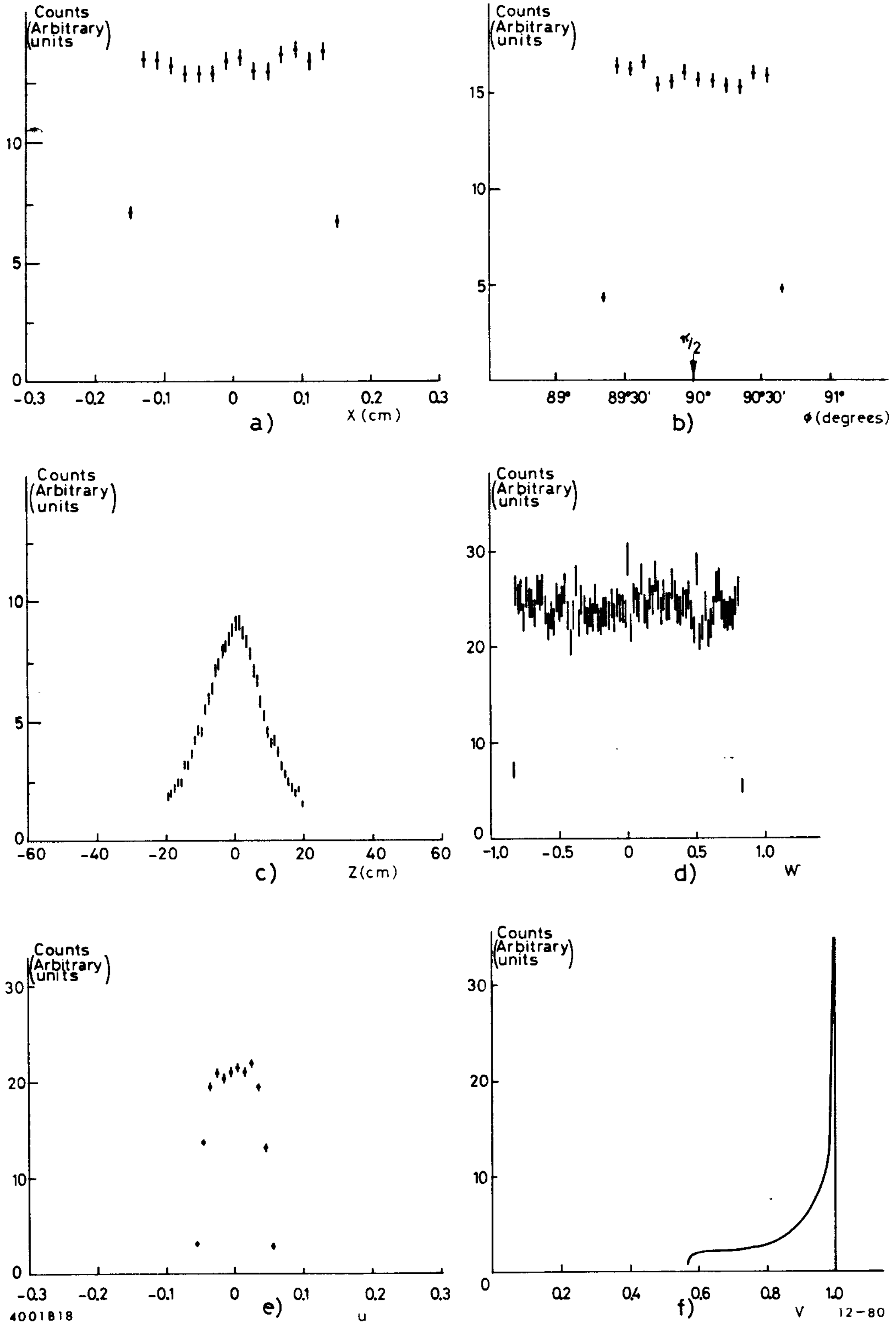
Counts (Arbitrary units)
0
5
10
-0.3
-0.2
-0.1
0
0.1
0.2
0.3
X (cm)
a)
Counts (Arbitrary units)
5
10
15
π/2
89°
89°30'
90°
90°30'
91°
b)
φ (degrees)
Counts (Arbitrary units)
0
5
10
-60
-40
-20
0
20
40
60
c)
Z(cm)
Counts (Arbitrary units)
0
10
20
30
-1.0
-0.5
0
0.5
1.0
d)
W
Counts (Arbitrary units)
0
10
20
30
-0.3
-0.2
-0.1
0
0.1
0.2
0.3
4001B18
e)
u
Counts (Arbitrary units)
0
10
20
30
0.2
0.4
0.6
0.8
1.0
f)
V
12-80

Fig. A.2

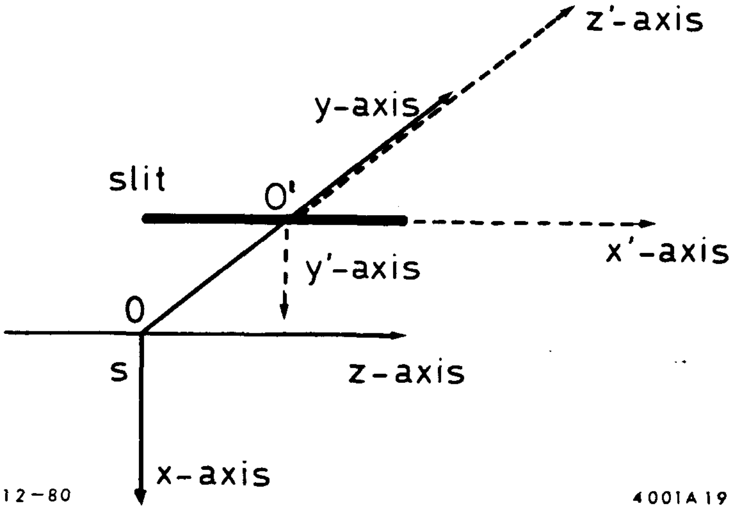

Fig. A.3

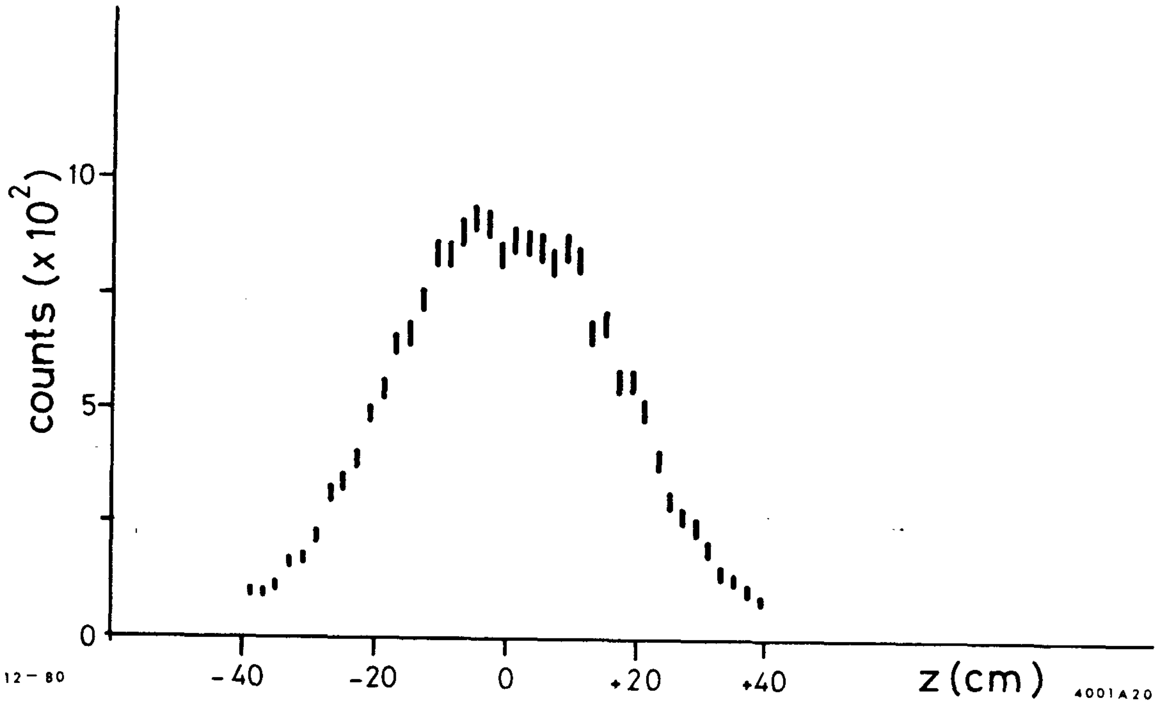

Fig. A.4